Check for updates

JGR Oceans

RESEARCH ARTICLE
10.1029/2022JC019375

Key Points:

- The Weddell Sea Bottom Water (WSBW) plume presents 3 velocity cores and a clear seasonal cycle, with maximum transports and densities in May and minimum in February
- A +SAM, reinforced by a -ENSO, favors the warming of WSBW via a wind-driven warming of the ambient waters entrained during its formation
- We observed a marked decrease in WSBW density and transports between September 2018 and February 2019 compared to the previous year

Supporting Information:

Supporting Information may be found in the online version of this article.

Correspondence to:

P. J. Llanillo,
pedro.llanillo@awi.de

Citation:

Llanillo, P. J., Kanzow, T., Janout, M. A., & Rohardt, G. (2023). The deep-water plume in the northwestern Weddell Sea, Antarctica: Mean state, seasonal cycle and interannual variability influenced by climate modes. *Journal of Geophysical Research: Oceans*, *128*, e2022JC019375. https://doi.org/10.1029/2022JC019375

Received 8 OCT 2022
Accepted 13 JAN 2023
Corrected 12 FEB 2023

This article was corrected on 12 FEB 2023. See the end of the full text for details.

© 2023. The Authors.
This is an open access article under the terms of the Creative Commons Attribution-NonCommercial-NoDerivs License, which permits use and distribution in any medium, provided the original work is properly cited, the use is non-commercial and no modifications or adaptations are made.

The Deep-Water Plume in the Northwestern Weddell Sea, Antarctica: Mean State, Seasonal Cycle and Interannual Variability Influenced by Climate Modes

Pedro J. Llanillo[1], Torsten Kanzow[1,2], Markus A. Janout[1], and Gerd Rohardt[1]

[1]Alfred-Wegener-Institute Helmholtz Center for Polar and Marine Research, Bremerhaven, Germany, [2]Department of Physics and Electrical Engineering, University of Bremen, Bremen, Germany

Abstract We provide an updated estimate of the annual-mean, seasonal cycle and interannual variability of the transports and properties of the Weddell Sea Bottom Water (WSBW) plume in the northwestern Weddell Sea. For this we used a densely instrumented mooring array deployed across the continental slope between January 2017 and January 2019. We found that the annual-mean WSBW transport is 3.4 ± 1.5 Sv, corresponding to a cross-section area of 35 km^2 and a maximum thickness of 203 m. The annual mean transport-weighted properties of WSBW are −0.99°C (Θ), 34.803 g/kg (SA) and 28.44 kg/m^3 (γ_n). The WSBW is characterized by 3 bottom-intensified velocity cores, which display seasonal variations in flow speed and transport different varieties of WSBW. The seasonal peak of WSBW transport and density is reached in May (4.7 Sv, 28.443 kg m^{-3}) while the minimum values are observed in February (2.8 Sv, 28.435 kg m^{-3}). The coldest WSBW is found between March and May, and the warmest between August and October. The density decrease of WSBW observed in the austral autumn of 2018 can be explained by warmer ambient waters being entrained during the formation of WSBW. This was enabled by the weakening of the along-shore winds associated with a positive Southern Annular Mode index, reinforced by a *La Niña* event in early 2018. The synchronous decrease of total WSBW transport and volume between September 2018 and February 2019 indicates a reduction in the export of the dense precursors of WSBW from the Weddell Sea continental shelf.

Plain Language Summary The Meridional Overturning Circulation (MOC) redistributes heat and carbon dioxide in the world ocean. Thus, it plays an important role in the regulation of our planet's climate. The Weddell Sea is the main contributor to the deep branch of the MOC in the Southern Hemisphere. Despite the importance of this contribution, uncertainties still remain associated to the plume of dense waters transported along the continental slope of the Weddell Sea. To reduce these uncertainties, we analyzed the most densely instrumented mooring array deployed across the continental slope in the northwestern Weddell Sea. We found that this plume flows faster close to the seafloor and that it presents important seasonal and interannual variability. The Weddell Sea Bottom Water interannual variability is influenced by changes in the along-shore winds driven by the phase of two important climate modes, the Southern Annular Mode and the El Niño-Southern Oscillation, but also by changes in the export of the dense precursors of WSBW in its formation areas. Increasing our knowledge on the along-slope plume variability and properties is important to better understand the causes behind the variability of the MOC observed further downstream.

1. Introduction

The lower limb of the Meridional Overturning Circulation (MOC) in the Southern Ocean is primarily fed by the dense waters originating from the Weddell Sea, followed in importance by the dense water supply in the Kerguelen Plateau (Fahrbach et al., 1995; Fukamachi et al., 2010; Orsi, 2010; Orsi et al., 1999; Warren, 1981). Intense surface cooling and brine rejection over the Weddell Sea continental shelf promotes a buoyancy loss of the Antarctic surface waters, which then sink and spread along the bottom of the continental shelf as High-Salinity Shelf Water (HSSW) (Gordon et al., 2001; Marshall & Speer, 2012; Orsi et al., 1999, 2001). The sinking of HSSW sequesters anthropogenic CO_2 from the atmosphere, and a fraction of it is later incorporated into the deep-water plume (Anderson et al., 1991; van Heuven et al., 2014). In some locations in the southern and southwestern Weddell Sea, the HSSW comes into contact with the under-side of floating ice-shelves inducing basal melting (Foldvik et al., 2004; Hellmer et al., 2017; Huhn et al., 2008; Jenkins, 1991). Through this ice-ocean interaction, the HSSW is transformed into Ice Shelf Water (ISW), which is characterized by slightly lower salinities and

21699291, 2023, 2, Downloaded from https://agupubs.onlinelibrary.wiley.com/doi/10.1029/2022JC019375 by Wiley, Wiley Online Library on [14/02/2023]. See the Terms and Conditions (https://onlinelibrary.wiley.com/terms-and-conditions) on Wiley Online Library for rules of use; OA articles are governed by the applicable Creative Commons License

temperatures below the surface freezing point of −1.9°C (Foldvik et al., 2004; Hellmer et al., 2012; Nicholls et al., 1991). Both HSSW and ISW are dense enough to sink to the bottom of the Weddell Sea, and when they cascade down the continental slope, they entrain and mix with Warm Deep Water (WDW) (Fahrbach et al., 1995; Gordon et al., 2001; Nicholls et al., 2009; Orsi et al., 1999). The entrainment of WDW within the cascading dense water plumes implies the transfer of oceanic heat into the deep ocean, being thus kept away from the ice shelves or the atmosphere (Fahrbach et al., 2011). The resulting deep-water plume, that initially cascades downslope, is progressively steered by the Coriolis effect until it flows along the bathymetry contours as part of the western boundary current of the Weddell Gyre (Gordon et al., 2001; Stommel, 1958; Stommel & Arons, 1959).

The densest water mass resulting from the entrainment of WDW by the dense water plumes exported down-slope is referred to as Weddell Sea Bottom Water (WSBW). The WSBW has previously been characterized either as the waters with a potential temperature (θ) of less than −0.7°C (Carmack & Foster, 1975a) or as the waters with a neutral density (γ_n) of at least 28.4 kg/m^3 (Fahrbach et al., 1995; Foldvik et al., 2004; Naveira Garabato et al., 2002). Above the WSBW, the Weddell Sea Deep Water (WSDW) is the result of further mixing between WSBW and WDW and comprises warmer and less dense waters (0°C > $\theta \geq$ −0.7°C, 28.27 kg/m^3 $\leq \gamma_n <$ 28.4 kg/m^3) (Fahrbach et al., 2001). Both WSBW and WSDW are transported northeastward by the deep western boundary current in the Weddell Gyre and, after further mixing with ambient waters, a fraction of them will eventually leak from the Weddell Basin northward into the south Scotia Sea and from there to the global ocean (Abrahamsen et al., 2019; Carmack & Foster, 1975b; Meijers et al., 2016; Meredith et al., 2011). The waters leaking from the Weddell Sea are referred as Antarctic Bottom Water (AABW), which then spreads equatorward as the lower limb of the MOC (Orsi et al., 1999; Reid & Lynn, 1971).

Despite the relevance of the Weddell Sea supply to the deep branch of the MOC (de Carvalho Ferreira & Kerr, 2017; Johnson, 2008), uncertainty still remains associated to its mean transports, spatial structure and variability along the Weddell Sea continental slope. This is mainly due to the data scarcity resulting from the logistically challenging Southern Ocean. In fact, the perennial sea-ice conditions on the western Weddell Sea, just upstream of our study area, have severely limited the amount of in situ scientific observations. The 1992 *Ice Station Weddell 1* program was the first successful attempt to investigate the hydrography and dynamics of the western Weddell Sea (Gordon, 1998; Gordon et al., 1993; Muench & Gordon, 1995). More than a decade later, this area was revisited in the framework of the *Ice Station POLarstern* (ISPOL, November 2004–January 2005), where the *RV Polarstern* drifted for about 290 km with an ice floe in the wider Larsen C ice shelf area (Absy et al., 2008; Hellmer et al., 2008). In addition, several cruises collected hydrographic data in the Northwestern Weddell Sea as part of the *International Deep Ocean Ventilation Through Antarctic Intermediate Layers* (DOVETAIL) program (Muench & Hellmer, 2002). The *RV Palmer* visited this region during the austral winter of 1997 (Gordon et al., 2001), while the *RV NApOc Ary Rongel* collected data during the austral summer of 2000 (Schröder et al., 2002). Furthermore, the *Polarstern* cruise ANT XXIX/3 occupied 3 cross-slope sections, ranging from the former locations of Larsen A and B ice shelves to the tip of the Antarctic Peninsula, in the late austral summer of 2013 (van Caspel et al., 2015).

Previous studies in the northwestern Weddell Sea were based on detailed shipboard snapshots (e.g., Thompson and Heywood, 2008) or employed the fewer moorings available historically to investigate the WSBW transports and properties (Fahrbach et al., 1995, 2001). From these studies, we learned that the plume can present distinct velocity cores (Fahrbach et al., 1995, 2001; Thompson & Heywood, 2008), and a plausible range of annual-mean WSBW transports (1.5–6 Sv). This range was derived from several scientific studies using either conductivity-temperature-depth (CTD) transects and moorings (Fahrbach et al., 2001; Foster & Carmack, 1976; Gordon et al., 1993), CTD and Lowered Acoustic Doppler Current Profiler (LADCP) sections (Gordon et al., 2001; Schröder et al., 2002), inverse models (Naveira Garabato et al., 2002) or moorings (Foldvik et al., 2004). Seasonal and interannual fluctuations of the WSBW plume were first estimated by Fahrbach et al. (2001). Moreover, Gordon et al. (2010) observed a seasonal cycle in the temperature of the WSBW plume at a mooring located further downstream at the slope of the South Orkney Plateau. They proposed that the seasonality in western Weddell Sea winds controls the export of dense shelf waters to the continental slope by depressing or raising the pycnocline at the shelf break, and thus, inducing the WSBW seasonal cycle that they observed in the South Orkney Plateau. Gordon et al. (2010) further suggested that the interannual variability of the WSBW also depends on variations in the volume of dense shelf waters exported downslope. These would be regulated by changing winds, influenced by the overlapping effects of the Southern Annular Mode (SAM) and El Niño/Southern Oscillation (ENSO) (Jullion et al., 2010; Martinson & Iannuzzi, 2003; McKee et al., 2011; Stammerjohn et al., 2008).

21699291, 2023, 2, Downloaded from https://agupubs.onlinelibrary.wiley.com/doi/10.1029/2022JC019375 by Wiley, Wiley Online Library on [14/02/2023]. See the Terms and Conditions (https://onlinelibrary.wiley.com/terms-and-conditions) on Wiley Online Library for rules of use; OA articles are governed by the applicable Creative Commons License

This study aims to provide updated estimates of the annual-mean and low-frequency variability of the WSBW plume and to investigate the plausible drivers behind its interannual variability. We first describe the annual-mean structure, transports and properties of the WSBW plume (Sections 4.1 and 4.2). Then, we investigate the difference between high and low transport events (Section 4.3). Next, we describe its seasonal cycle (Section 4.4) and interannual variability (Section 4.5). Subsequently, we discuss how our results compare to previous studies and the drivers that might cause the observed interannual variability of WSBW (Section 5). We finish with a short summary and the main conclusions (Section 6).

2. Data

Seven moorings (NW1–NW7), spaced 35–50 km apart, were installed along a 250 km transect across the continental slope of the NW Weddell Sea between January 2017 and January 2019 (Figure 1) within the framework of Hybrid Antarctic Float Observation System, a long-term observational effort lead by the Alfred Wegener Institute (AWI). These moorings were deployed and recovered during *RV Polarstern* expeditions PS103 and PS117 respectively (links to cruise reports available from the Open Research Section). All moorings were equipped with 3 Aanderaa current meters (models RCM7, RCM8 and RCM11), 3 Seabird MicroCAT CTD sensors (SBE37) and 3 Seabird temperature-depth recorders (SBE39/56). Their spatial disposition can be examined in Figure 2, while their specific details are provided in Table S1.

The RCMs have an accuracy of ±1 cm/s for speed and ±5° for direction. The accuracy of the SBE37 sensors is ±0.002°C for temperature (T), ±0.003 mS/cm for conductivity (C) and ±0.1% for pressure (P). Moreover, the SBE39 have an accuracy of ±0.1% for P and the SBE39/56 sensors present an accuracy of ±0.002°C for T. Further details can be found in the PS103 and PS117 cruise reports.

Before deployment and after recovery, the SBE37 and SBE39/56 sensors were mounted on the CTD-rosette (SBE 911+) for an inter-calibration cast in which they were kept for about 5 min within a homogeneous ocean layer. In addition, the conductivity measurements of the SBE 911+ were corrected using an Optimare Precision Salinometer on board the *RV Polarstern*. During the post-processing, ship-based CTD profiles were used to further inspect the existence of drifts and/or offsets in the moored data set.

The details of the moored instruments employed to create the long historical timeseries (2005–2022) of thermohaline properties at the bottom of NW3 are provided in Supporting Information S1 (Table S2). This data set resulted from *RV Polarstern* expeditions ANT-XXII, ANT-XXVII, PS103 and PS129 (cruise reports linked in the Open Research Section).

3. Materials and Methods

The data from failing instruments were reconstructed whenever it was possible (Table S3). As the distance between our moorings is larger than the first baroclinic Rossby radius of deformation for these latitudes (10–15 km), the mesoscale activity is not well resolved by our measurements. Thus, the data set was low-pass filtered, with a 5th order Butterworth filter and a 30 days cutoff, in order to remove any mesoscale, tidal and internal wave influence. Subsequently, all data were linearly interpolated on a common 12-hourly time vector. Note that throughout the paper the salinity is given as absolute salinity (SA) and the temperature as conservative temperature (Θ), both were computed using the TEOS-10 Gibbs thermodynamic potential for seawater toolbox (McDougall & Barker, 2011).

In order to extend the property profiles down to the seafloor, we replicated at the sea floor the data measured in each mooring by its bottom most instrument, which was located less than 10 m above the seafloor. This is justified by the existence of a well-mixed bottom boundary layer in this location (Fahrbach et al., 2001). Then, the data was vertically interpolated with a piecewise cubic Hermite interpolating polynomial (pchip) at a vertical resolution of 10 m. Subsequently, the data set was horizontally interpolated onto a grid at 1 km resolution with the vertical coordinate being the height above the seafloor instead of the water depth. Horizontal linear extrapolation beyond NW1 and NW7 was only allowed for 25 km on both sides of the grid and for 50 m above the uppermost instrument in the vertical. Then, the component of the velocity perpendicular to the moorings transect (i.e., the along slope component) was computed and volume transports were obtained by integrating the velocity vectors multiplied by the area of each grid cell within the cross-section area of WSBW in the transect defined by the moorings array.

21699291, 2023, 2, Downloaded from https://agupubs.onlinelibrary.wiley.com/doi/10.1029/2022JC019375 by Wiley, Wiley Online Library on [14/02/2023]. See the Terms and Conditions (https://onlinelibrary.wiley.com/terms-and-conditions) on Wiley Online Library for rules of use; OA articles are governed by the applicable Creative Commons License

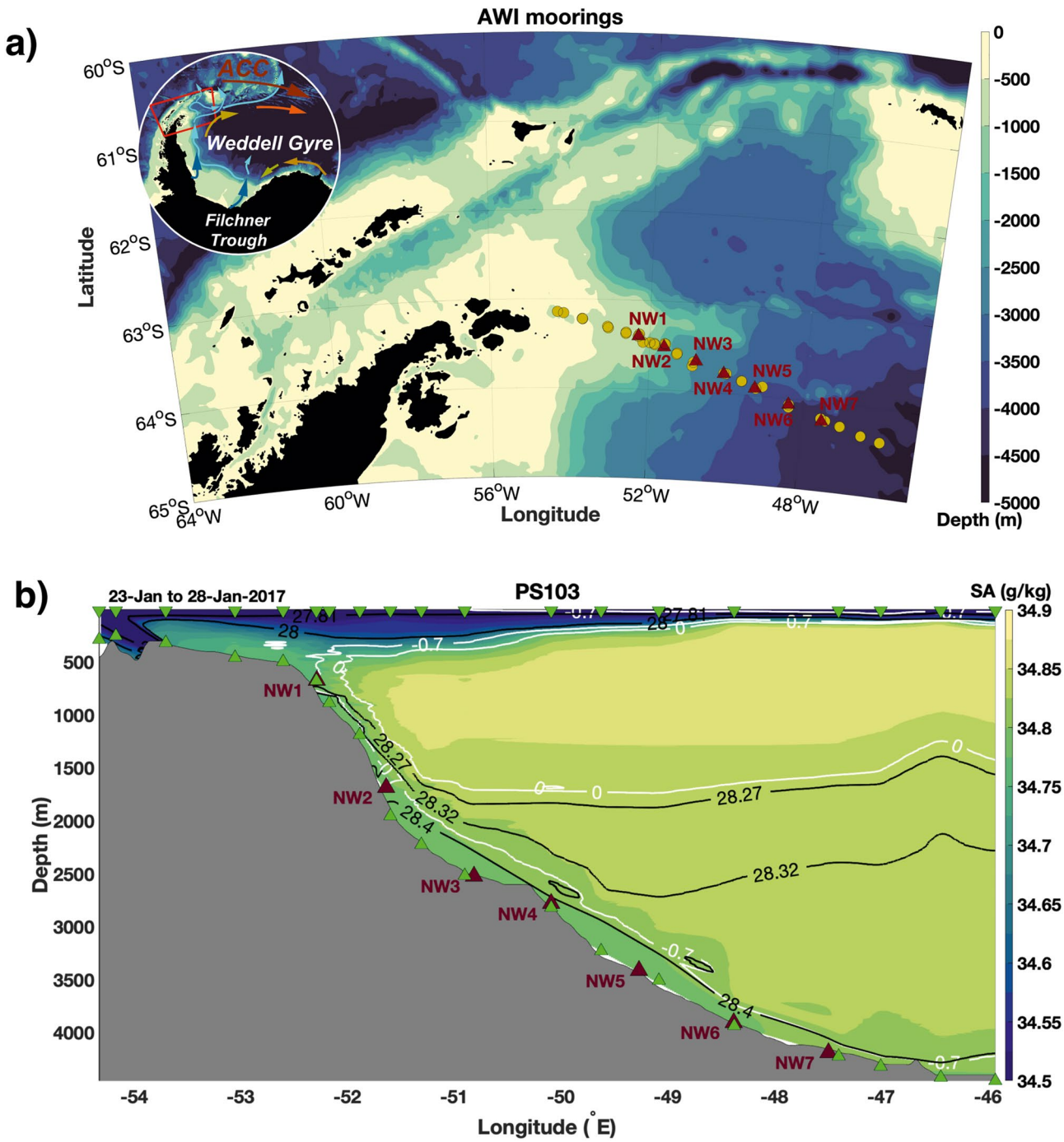

Figure 1. (a) Map of the NW Weddell Sea with the 2017–2019 Alfred Wegener Institute (AWI) mooring array (maroon triangles) and the conductivity-temperature-depth (CTD) stations sampled during deployment and recovery cruises (yellow dots). The bathymetry from ETOPO-2 is color coded. The insert shows the Weddell Gyre circulation, the export of dense shelf waters from the Filchner Trough and in front of the Larsen Ice Shelf (dark blue arrows) and the main paths of the exported dense waters (light blue arrows). (b) Transect across the continental slope showing the location of the 2017–2019 AWI mooring array (maroon triangles) and CTD stations obtained during the deployment cruise (PS103, green triangles). Absolute salinity (SA; g/kg) measured during PS103 is depicted (color coded), with overlying isoneutrals (black contours) and isothermals (white contours). The bathymetry is from BEDMAP-2 (1 km resolution).

Thresholds based on either θ (<−0.7°C) or γ_n (≥28.4 kg/m^3) have been previously employed to delimit the WSBW (Fahrbach et al., 1995, 2001; Gordon et al., 2001; Naveira Garabato et al., 2002). In order to enable comparison with historical estimates, we computed the WSBW annual-mean values with both thresholds. Note that we use Θ instead of θ to characterize the WSBW, but the corresponding Θ value only differs in 0.0002°C

21699291, 2023, 2, Downloaded from https://agupubs.onlinelibrary.wiley.com/doi/10.1029/2022JC019375 by Wiley, Wiley Online Library on [14/02/2023]. See the Terms and Conditions (https://onlinelibrary.wiley.com/terms-and-conditions) on Wiley Online Library for rules of use; OA articles are governed by the applicable Creative Commons License

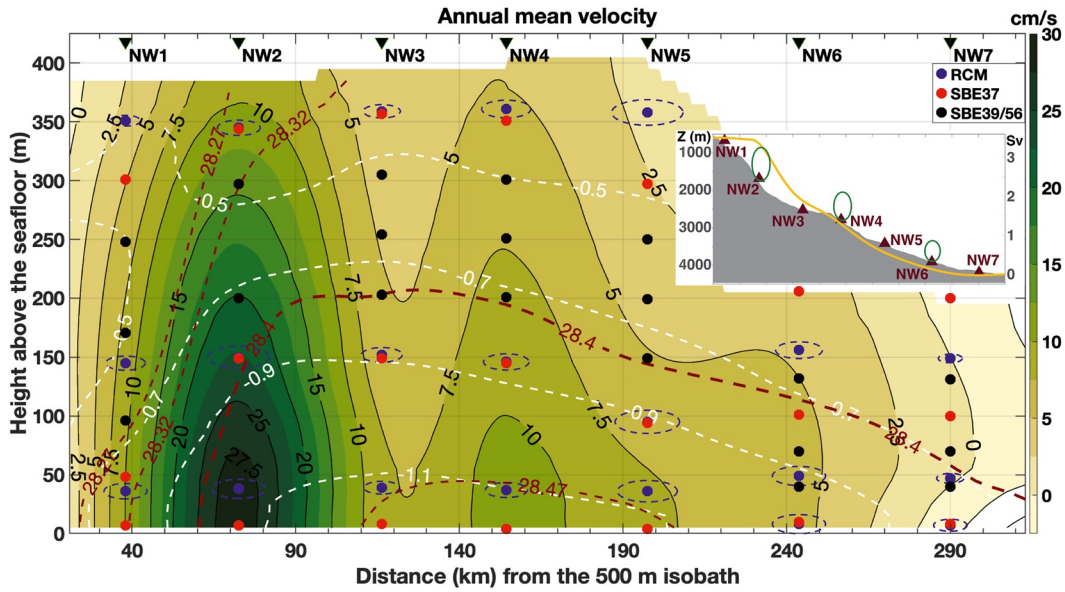

Figure 2. Annual mean fields of along-slope velocity (color coded and black contours), neutral density (maroon contours) and conservative temperature (white contours). The standard deviation of the velocities measured in each current-meter (RCM) is represented by the size of the horizontal axis of the blue ellipses. The moorings location (black triangles) and the spatial distribution of the instruments employed is also indicated. The horizontal axis indicates the distance off-shore from the 500 m isobath. The insert shows the bathymetric profile, the mooring positions (triangles), the velocity cores (green ovals) and the cumulative annual-mean transports (Sv) from the deepest to the shallowest mooring (yellow line).

from the θ threshold. The WSBW cross-section area and transports are always larger when using the Θ threshold to delimit WSBW than when using the γ_n threshold. Note that from Section 3.3 onwards, we will only discuss the results obtained when using a γ_n boundary, as this threshold is the only one that enables separating the WSBW from the Winter Water in the upper reaches of the continental slope.

The uncertainty associated with the computed WSBW transports was calculated by considering the standard error of the transports, together with the uncertainty in the estimation of the cross-section areas, obtained from a comparison with CTD transects, and the uncertainty associated to the velocity measurements. These sources of error were combined by means of classical error propagation formula into a global estimate of the uncertainty associated to the computed transports ($\pm$1.5 Sv for a γ_n boundary; $\pm$1.1 Sv for a Θ boundary).

We composited the low-pass filtered data set according to the WSBW transports measured in each time step into a high-transport composite (selecting the time steps with WSBW transports exceeding the annual-mean transport plus one standard deviation, i.e., >4.2 Sv) and a low-transport composite (same but for the time steps with WSBW transports smaller than the annual-mean minus one standard deviation, i.e., <2.6 Sv). We subsequently averaged separately the high and low-transport events, in order to obtain representative mean properties for the high- and low-transport composites.

To obtain the seasonal fit for the WSBW transports and cross-section areas (red line in Figure 3), we first smoothed the 30 days low-pass filtered timeseries with a 15 days moving-average window. Then, the smoothed timeseries were detrended and, finally, the corresponding values for each day of the year were averaged between the different years in record. On the other hand, the seasonal property fields discussed in Section 4.4 were obtained by detrending and then averaging the low-pass filtered data for each month of the year between the different years in record.

For the analysis of the WSBW interannual variability, we constructed a long historical time series between March 2005 and April 2022 with the thermohaline data from mooring NW3 (officially termed AWI-207), maintained by the AWI. We particularly focused on the properties recorded by the bottom MicroCAT (SBE37) in each redeployment, as they are expected to capture more precisely the variability of the bottom-intensified WSBW plume (Table S2 in Supporting Information S1).

In addition, we constructed a new climate index, the SAM-ENSO index (SEI), that combines the SAM index (Marshall, 2003) with the Oceanic Niño Index (ONI) (Bamston et al., 1997; Huang et al., 2016), and takes into

21699291, 2023, 2, Downloaded from https://agupubs.onlinelibrary.wiley.com/doi/10.1029/2022JC019375 by Wiley, Wiley Online Library on [14/02/2023]. See the Terms and Conditions (https://onlinelibrary.wiley.com/terms-and-conditions) on Wiley Online Library for rules of use; OA articles are governed by the applicable Creative Commons License

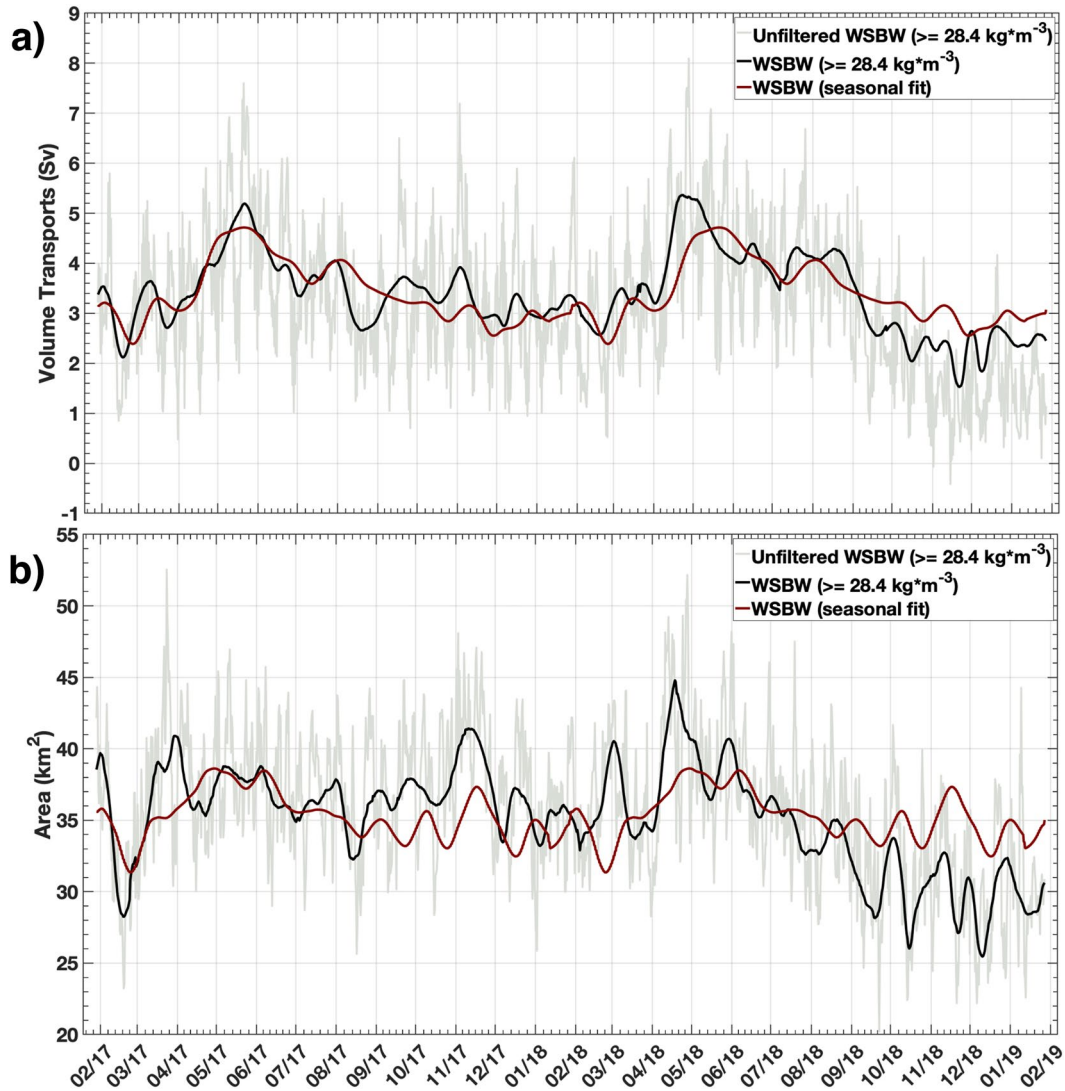

Figure 3. Time series of the Deep Water Plume (Weddell Sea Bottom Water) (30 day low-pass filtered: black line, unfiltered: gray line). Superimposed is the seasonal fit (red line, see Section 3) for (a) Volume transport (Sv) and (b) Cross-section area (km^2).

account their overlapping effects on the wind field around Antarctica (discussed in Section 5.4). The SEI is available in the Open Research Section and was computed as follows:

$$\mathrm{SEI} = \frac{\mathrm{SAM}}{\mathrm{std(SAM)}} - \frac{\mathrm{ONI}}{\mathrm{std(ONI)}}$$

To further inspect the interannual changes in WSBW, we divided this water mass into 3 different neutral density subclasses (densest: $28.47 \leq \gamma_n < 28.60$ kg m^{-3}; intermediate: $28.44 \leq \gamma_n < 28.47$ kg m^{-3} and lightest: $28.40 \leq \gamma_n < 28.44$ kg m^{-3}).

4. Results

4.1. Annual-Mean Spatial Structure of the WSBW Plume

The WSBW plume stretches for roughly 260 km considering the γ_n boundary, but reaches at least 35 km further upslope of mooring NW2 when using the Θ boundary (Figure 2). We observed that the maximum annual-mean plume thickness (203 m) is located at mooring NW3 (named as AWI-207 in Fahrbach et al. (2001)), although

21699291, 2023, 2, Downloaded from https://agupubs.onlinelibrary.wiley.com/doi/10.1029/2022JC019375 by Wiley, Wiley Online Library on [14/02/2023]. See the Terms and Conditions (https://onlinelibrary.wiley.com/terms-and-conditions) on Wiley Online Library for rules of use; OA articles are governed by the applicable Creative Commons License

the plume is only 10 m thinner at mooring NW4. On the upper slope, between moorings NW1 and NW2, strong downslope gradients of γ_n, Θ and SA indicate the transition between shelf waters, modified by mixing with WDW, and WSDW and WSBW (Figure 2).

The along-slope velocities decrease progressively upward from the sea floor and toward the base of the continental slope, with annual-mean along-slope velocities indicating zero flow in the southeasternmost mooring (NW7) deployed at the 4,170 m isobath. There are three bottom-intensified cores of along-slope velocity, each separated by approximately 90 km from the next one (Figure 2). The highest annual-mean velocities (28.6 cm/s) are found in the first core located at mooring NW2 on the upper continental slope at the 1,660 m isobath (Figure 2). This core is located at the western and shallower boundary of the WSBW, where the steepness of the bathymetric slope is largest (Figure 1b). The second velocity core is weaker and narrower, with a maximum annual-mean flow of 11.1 cm/s, and is located in the center of the WSBW at the 2,760 m isobath (mooring NW4, Figure 2). Note that the first core is characterized by a significantly larger vertical velocity shear than the lower core, and it is probably strengthened by the larger horizontal density gradient resulting from the horizontal transition between the dense WSBW and the less dense WDW found offshore (Figure 1b). A weaker third velocity core, with annual-mean velocities below 7.5 cm/s, can be partially observed centered in mooring NW6 at 3.880 m depth (Figure 2). As shown later, this core is not clearly discernible during some months of the year. The largest variability of the along-slope velocities is found outside of these 3 velocity cores in the mooring NW5, which was deployed at the 3,390 m isobath (variance ellipses in Figure 2).

4.2. Annual-Mean WSBW Plume Transport and Properties

The annual-mean WSBW transport along the NW Weddell Sea continental slope is 3.4 ± 1.5 Sv, corresponding to an annual-mean cross-section area of ~35 km^2 when using a γ_n boundary (Figure 2). The corresponding values are larger (4.7 ± 1.1 Sv, 45 km^2) when using the Θ boundary. Nevertheless, pronounced fluctuations at monthly, seasonal and interannual timescales are superimposed on these annual-mean values. Specifically, WSBW transports (areas) oscillate between a minimum of 1.5 Sv and a maximum of 5.4 Sv (25.5–44.8 km^2), with a standard deviation of ±0.78 Sv (±3.65 km^2) when using the γ_n boundary (Figure 3). For the Θ boundary, the values fluctuate between 2.7 and 7.0 Sv (37.8–54.9 km^2), with a standard deviation of ±0.86 Sv (±3.81 km^2).

As the WSBW has a bottom-intensified flow, using transport-weighted properties enables a more accurate description of the properties effectively transported by the WSBW. The annual-mean transport-weighted WSBW properties with the γ_n boundary (Θ boundary) are $\Theta_w = -0.99$ (−0.94)°C, $SA_w = 34.803$ (34.801) g/kg and 28.44 (28.42) kg/m^3 respectively. While Θ_w and SA_w display a strong positive correlation of 0.84 (0.59) between each other, the Θ_w and the WSBW transports present a weak negative correlation of −0.19 (−0.37), while the SA_w shows no correlation with the WSBW transports, with a value of 0.08 (0.19) (Figure 4).

4.3. Contrasting Spatial Patterns Between High-Transport and Low-Transport Events

After investigating the annual-mean properties, we now take a look into patterns of temporal variability of the WSBW transports. For this, we created high- and low-transport composites (see Section 3). The average WSBW transport of the high-transport composite is 4.7 Sv (2.3 Sv for the low-transport) with an average cross-section area of 38.1 (29.6) km^2. The along-slope velocities show a coherent increase across the entire WSBW plume in the high-transport composite (Figure 5a), with two regions showing the most pronounced velocity increases. The first region is centered at mooring NW2, where the most intense velocity core is found, and presents large velocity anomalies (>5 cm/s) in the bottom 250 m. The second region with a pronounced velocity anomaly (>4 cm/s), comprises the third velocity core (NW6), and the transition zone (NW5) between the second (NW4) and third velocity cores (Figure 5a). Outside of these two maxima, typical velocity anomalies amount to 3 cm/s.

During high-transport events (Figure S1 in Supporting Information S1), the WSBW is slightly more saline near the bottom in the western and central regions, between NW1 and NW5, and slightly fresher in the east between NW5 and NW7 (Figure 5b). The maximum positive salinity anomaly (+0.007 g/kg) is found near the bottom at NW4 within the second velocity core. The largest negative salinity anomaly (−0.006 g/kg) is found at the bottom-most 100 m of NW6, coincident with the third velocity core. This indicates that during low-transport events (Figure S2 in Supporting Information S1), the WSBW is slightly more saline in the third velocity core region, likely as a result of the larger influence of the more saline waters occupying the interior of the Weddell Gyre (Figure 5b).

21699291, 2023, 2, Downloaded from https://agupubs.onlinelibrary.wiley.com/doi/10.1029/2022JC019375 by Wiley, Wiley Online Library on [14/02/2023]. See the Terms and Conditions (https://onlinelibrary.wiley.com/terms-and-conditions) on Wiley Online Library for rules of use; OA articles are governed by the applicable Creative Commons License

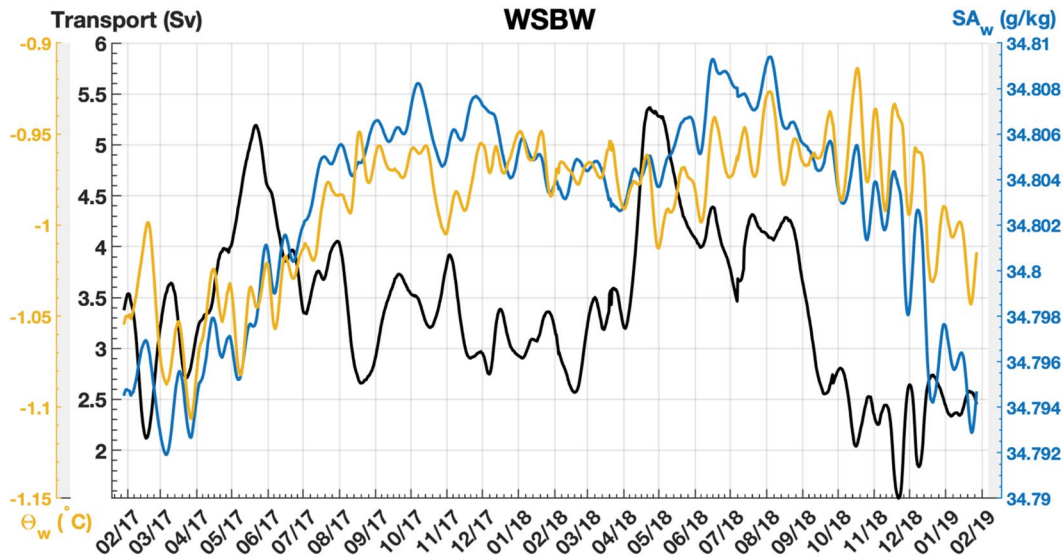

Figure 4. Volume transports (Sv, black line) and transport-weighted conservative temperature (°C, yellow line) and absolute salinity (g/kg, blue line) of Weddell Sea Bottom Water when defined by a neutral density threshold.

4.4. Seasonal Cycle of WSBW Transports and Properties

The WSBW transports and cross-section areas peak in May, with 4.65 Sv and 37.9 km^2 respectively, decreasing thereafter until November. Then, they increase slightly until January, reaching their minimum values in February (2.8 Sv, 33.4 km^2). After February, the WSBW transports and areas increase again until May (Figure 6 and Table S4 in Supporting Information S1). On the other hand, the mean WSBW along-slope velocities increase progressively from a secondary minimum in February until May, when they reach a maximum value of 12.2 cm/s. After May, the mean WSBW velocity decreases again to a minimum in November (Figure 6, Table S4 in Supporting Information S1). Note that the seasonal along-slope velocity is 50% larger in May than in February, and dominates the seasonality in WSBW transports rather than the cross-section area (which shows peak-to-peak changes of 15%). In November, a secondary maximum of WSBW cross-section area partially compensates for the minimum along-slope velocity (7.7 cm/s), making the WSBW transport in November slightly larger than in February (Table S4 in Supporting Information S1). The plausible causes behind this will be examined later in the discussion section.

The transport-weighted γ_n of WSBW is minimum in February (28.435 kg m^{-3}), coincident with the minimum in WSBW cross-section area and transport. After February, the γ_n of WSBW progressively increases, reaching a maximum value in May/June (28.443 kg m^{-3}). Thereafter it decreases until September (28.437 kg m^{-3}), increasing very slightly in October and November, and decreasing again from December until February (Figure 6, Table S4 in Supporting Information S1). The Θ_w of WSBW is coldest in March (−1.01°C), and stays especially low between January and May, increasing then until August (−0.97°C), and decreasing thereafter. There is a clear freshening of the upper-slope velocity core between December and March. This indicates mixing with fresh shelf waters during the austral summer. Thus, the minimum SA_w of WSBW is attained in January (34.799 g/kg), while SA_w stays in low values (<34.802 g/kg) between December and April, increasing subsequently until July/August (34.806 g/kg) and decreasing thereafter. These results indicate that the seasonal cycle of Θ_w and SA_w are not aligned with the seasonal cycle of the transport-weighted γ_n within the WSBW (Figure 6, Table S4 in Supporting Information S1).

The WSBW reaches its maximum thickness in May, with ∼225 m at mooring NW3, when only two bottom-intensified velocity cores are visible (Figure 7a). The upper-slope core, centered in NW2, is more intense (32.1 cm/s) and slightly fresher (∼34.79 g/kg) than the second core (14.7 cm/s, ∼34.80 g/kg), which transports the densest variety of WSBW (Figures 2 and 8). From May to August, the WSBW cross-section areas and velocities decrease progressively and the WSBW becomes warmer and more saline (Figures 7a and 7b, Table S4 in Supporting Information S1). This progressive decrease in along-slope velocities reveals the presence of the third velocity core centered at NW6 (Figure 7b), clearly visible from August to December, when its velocity peaks at

21699291, 2023, 2, Downloaded from https://agupubs.onlinelibrary.wiley.com/doi/10.1029/2022JC019375 by Wiley, Wiley Online Library on [14/02/2023]. See the Terms and Conditions (https://onlinelibrary.wiley.com/terms-and-conditions) on Wiley Online Library for rules of use; OA articles are governed by the applicable Creative Commons License

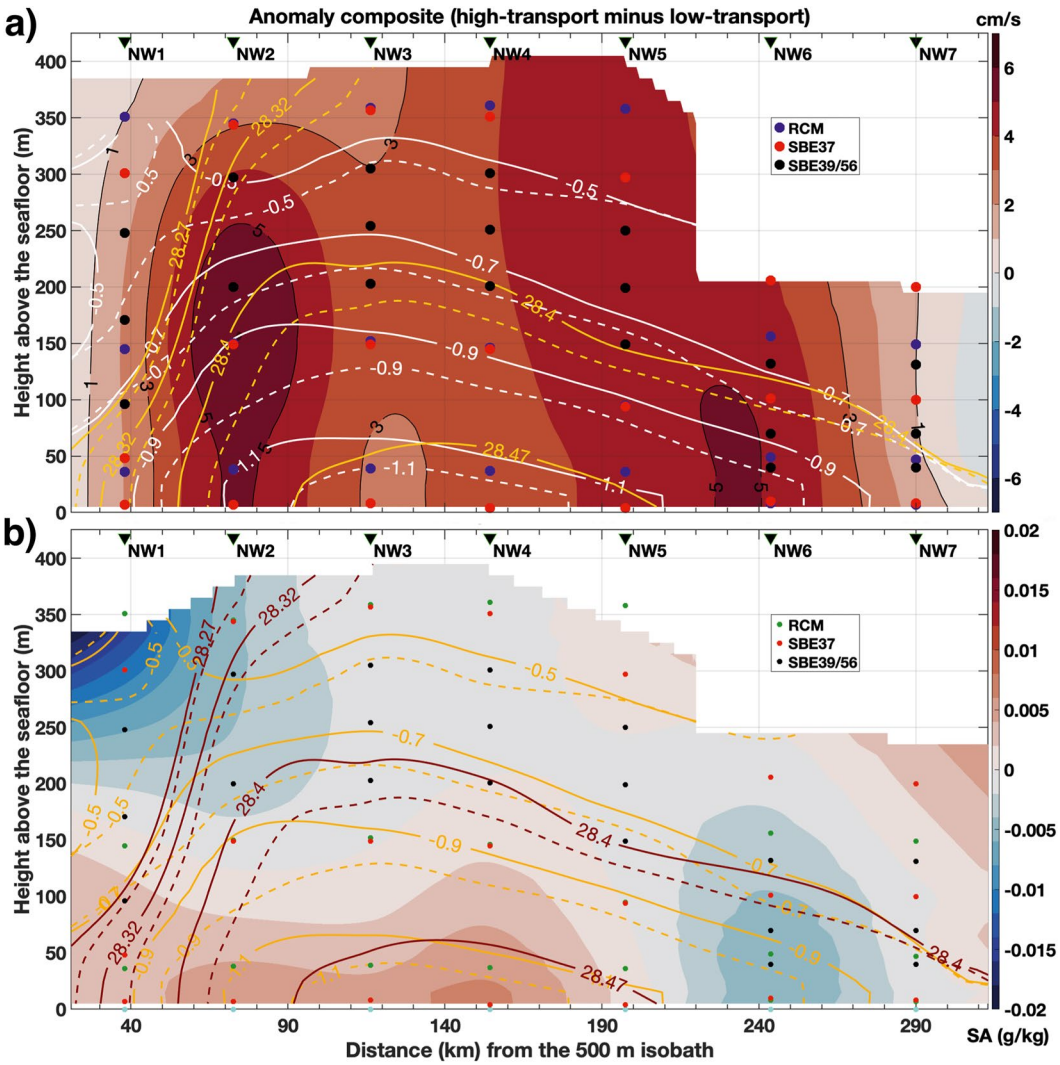

Figure 5. Anomaly fields (high-transport minus low-transport composites) of (a) along-slope velocity (cm/s) and (b) absolute salinity (g/kg) (with their anomalies color coded). The isolines of neutral density and conservative temperature represent the high-transport (straight lines) and the low-transport (dashed lines) composites. The moorings location (black triangles) and the spatial distribution of instruments is also indicated. The horizontal axis indicates the distance off-shore from the 500 m isobath.

11.7 cm/s (Figure 8). From February to May, the first and second velocity cores intensify, resulting in the merging of the second and third velocity cores. This increase is more intense between April and May, when the pulse of the newly exported WSBW arrives to the NW Weddell Sea. During these months, the WSBW in these velocity cores becomes colder, denser and slightly saltier.

4.5. Interannual Changes in WSBW Density

The three WSBW density subclasses (defined in Section 3) increase their volume transports during the pulse of new WSBW arriving between April and June (AMJ) each year. However, these subclasses present different year-to-year variability. While the maximum volume transported by the densest subclass decreased in AMJ 2018 with respect to the same period in 2017 (from 1.26 to 0.98 Sv); the other two subclasses increased their maximum volume transports (Figure 9a). Especially the less dense subclass, which transported a maximum of 3.17 Sv in AMJ 2018 compared to a maximum of 2.49 Sv transported in AMJ 2017. The intermediate subclass showed a smaller increase in its maximum volume transport (from 1.75 to 1.99 Sv). As the decrease in the transports of the densest subclass is compensated by an increase in the transports of the lighter subclasses, we measured very

21699291, 2023, 2, Downloaded from https://agupubs.onlinelibrary.wiley.com/doi/10.1029/2022JC019375 by Wiley, Wiley Online Library on [14/02/2023]. See the Terms and Conditions (https://onlinelibrary.wiley.com/terms-and-conditions) on Wiley Online Library for rules of use; OA articles are governed by the applicable Creative Commons License

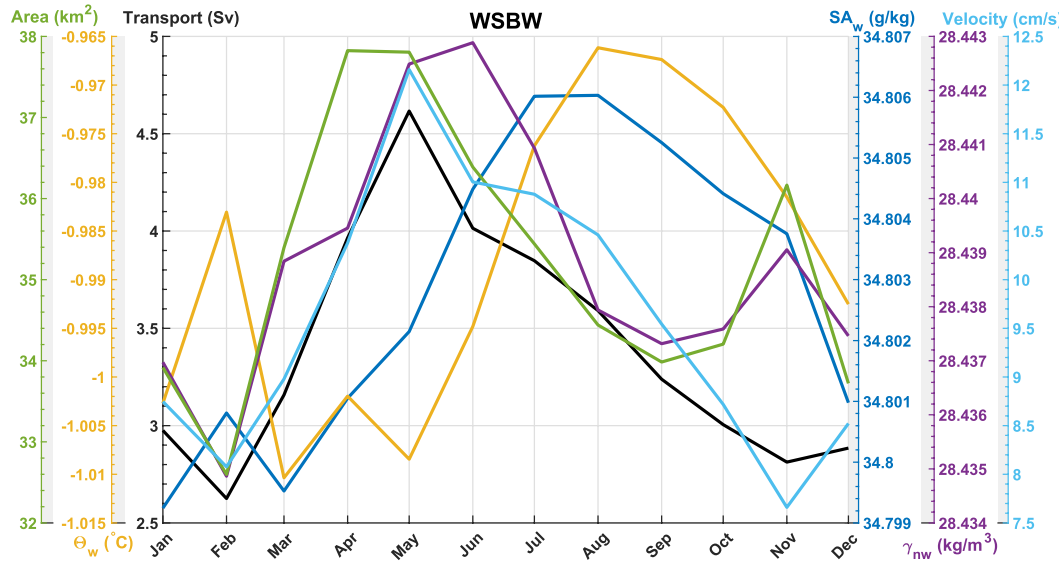

Figure 6. Seasonal cycle of Weddell Sea Bottom Water (WSBW) transports (Sv, black line), cross-section area (km^2, green line), cross-section velocities (cm/s, cyan line), and transport-weighted WSBW neutral density anomaly (γ_n, in kg m^{-3}, purple line), conservative temperature (Θ_w, in °C, yellow line) and absolute salinity (SA_w, in g/kg, dark blue line). The values shown here are obtained after low-pass filtering the data with a 30 days cutoff period. The corresponding numeric values are presented in Table S4 in Supporting Information S1.

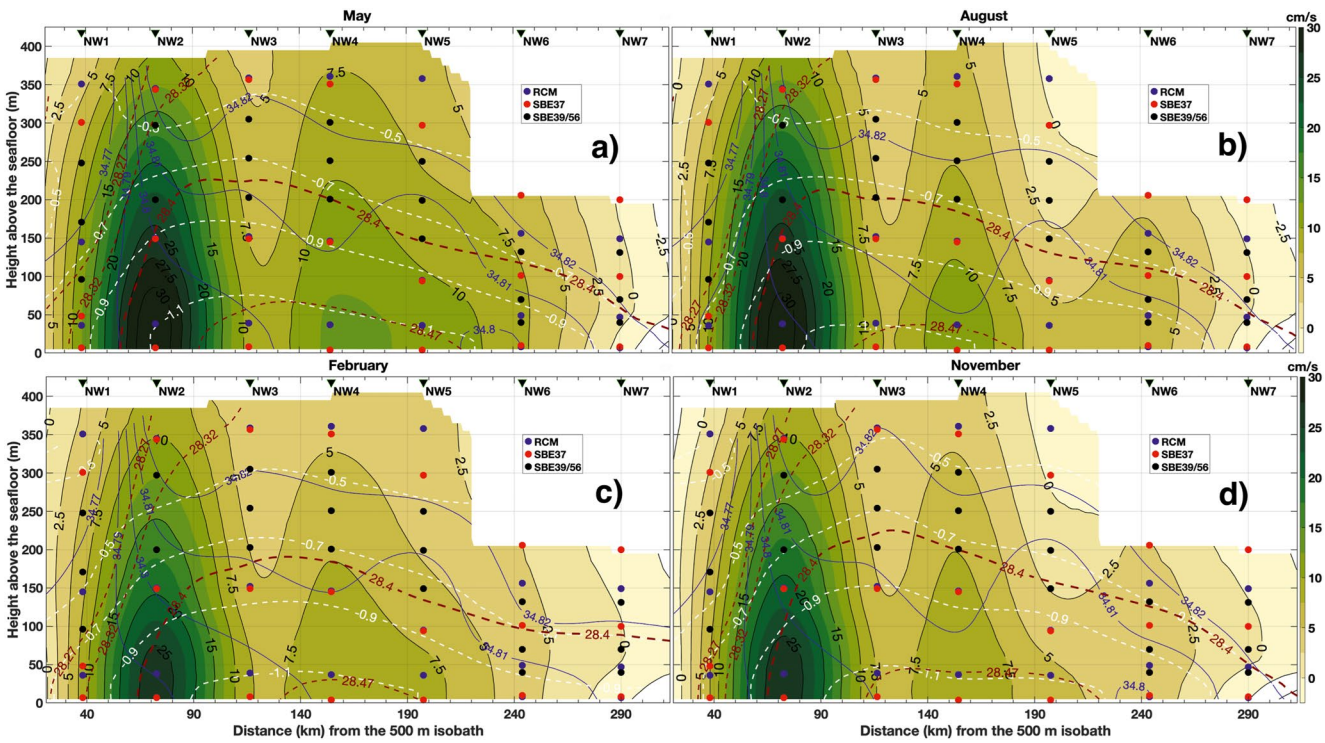

Figure 7. Average fields of along-slope velocity (color coded and black contours), neutral density (maroon contours), absolute salinity (blue contours) and conservative temperature (white contours) during (a) the month with maximum Weddell Sea Bottom Water (WSBW) transports (May), (b) the month with the 3 velocity cores clearly observed (August) (c) the month with minimum WSBW transports (February) and (d) the month with the minimum WSBW along-slope velocity (November). The moorings location (black triangles) and the spatial distribution and type of instruments is also indicated. The horizontal axis indicates the distance off-shore from the 500 m isobath.

21699291, 2023, 2, Downloaded from https://agupubs.onlinelibrary.wiley.com/doi/10.1029/2022JC019375 by Wiley, Wiley Online Library on [14/02/2023]. See the Terms and Conditions (https://onlinelibrary.wiley.com/terms-and-conditions) on Wiley Online Library for rules of use; OA articles are governed by the applicable Creative Commons License

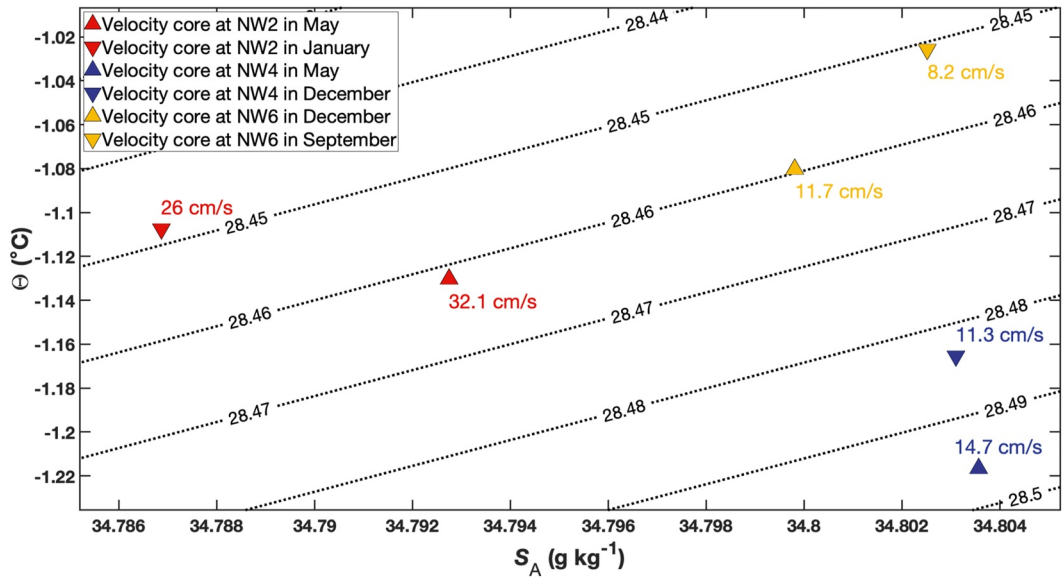

Figure 8. Conservative Temperature (Θ, ºC)—Absolute Salinity (S_A, g/kg) diagram showing the characteristic thermohaline properties of the first (red triangles), second (blue triangles) and third (yellow triangles) velocity cores at the month of their maximum (up-looking triangles) and minimum (down-looking triangles) speed (cm/s). Neutral density (γ_n, kg/m^3) contours are indicated by the black dotted lines.

similar transports peaks of WSBW in 2017 (5.19 Sv) and 2018 (5.37 Sv) (Figure 9a). The observed decrease in the densest WSBW subclass might be explainable either by a decrease in the density of its dense precursors (i.e., ISW, HSSW), or by the entrainment of warmer and saltier ambient waters (WDW) during the downslope descent of the dense plumes of WSBW precursors. The plausibility of these two hypotheses will be explored in the Discussion Section.

Before that, we describe here how the transport-weighted thermohaline properties of WSBW (Figure 4) and of its subclasses (Figures 9b and 9c) differed between these two annual WSBW transport peaks, which occurred on the 23 April 2018 (A18) and on the 21 May 2017 (M17) respectively. Note that the following values were obtained by averaging the transport-weighted thermohaline properties in the 2 days before and after the peak in WSBW transports. During the A18 transport peak, the WSBW was characterized by a SA_w of 34.805 g/kg and a Θ_w of −0.97°C, while in the M17 peak it was fresher (34.798 g/kg) and colder (−1.04°C). Furthermore, the three WSBW subclasses were saltier and warmer during A18 than during M17 (Figures 9b and 9c). Specifically, the less dense subclass was 0.008 g/kg saltier and 0.05°C warmer, the intermediate subclass was 0.006 g/kg saltier and 0.03°C warmer; and the densest subclass was 0.005 g/kg saltier and 0.04°C warmer. The fact that the warming and gain in salinity is larger in the less dense subclass, suggests that a less modified WDW was entrained during the formation of WSBW in early 2018 (see the Discussion Section).

Three months after the changes described above, our records indicate a reduction of the total WSBW transports (~30%) and cross-section areas (~20%) during the austral spring and summer of 2018–2019, compared to the same period in the previous year (Figure 9a). Specifically, from 3.27 Sv/36.9 km^2 (September 2017–February 2018) to 2.47 Sv/29.9 km^2 (September 2018–February 2019). Furthermore, the three WSBW subclasses showed a transport decrease, with most of this decrease taking place in the intermediate (from 1.18 to 0.84 Sv) and densest (from 0.39 to 0.08 Sv) subclasses. They also presented a decrease in their average areas, with the densest subclass showing the largest decrease (from 4.6 to 0.8 km^2), followed by the intermediate subclass (from 12.1 to 9.4 km^2) and the less dense subclass (from 20.2 to 19.7 km^2). In addition the three subclasses show a marked salinity decrease during this period in comparison to the previous year. The observed synchronous decrease in WSBW transports and areas might be explained by a reduced export of the dense precursors of WSBW (Janout et al., 2021) (more on this in the Section 5).

21699291, 2023, 2, Downloaded from https://agupubs.onlinelibrary.wiley.com/doi/10.1029/2022JC019375 by Wiley, Wiley Online Library on [14/02/2023]. See the Terms and Conditions (https://onlinelibrary.wiley.com/terms-and-conditions) on Wiley Online Library for rules of use; OA articles are governed by the applicable Creative Commons License

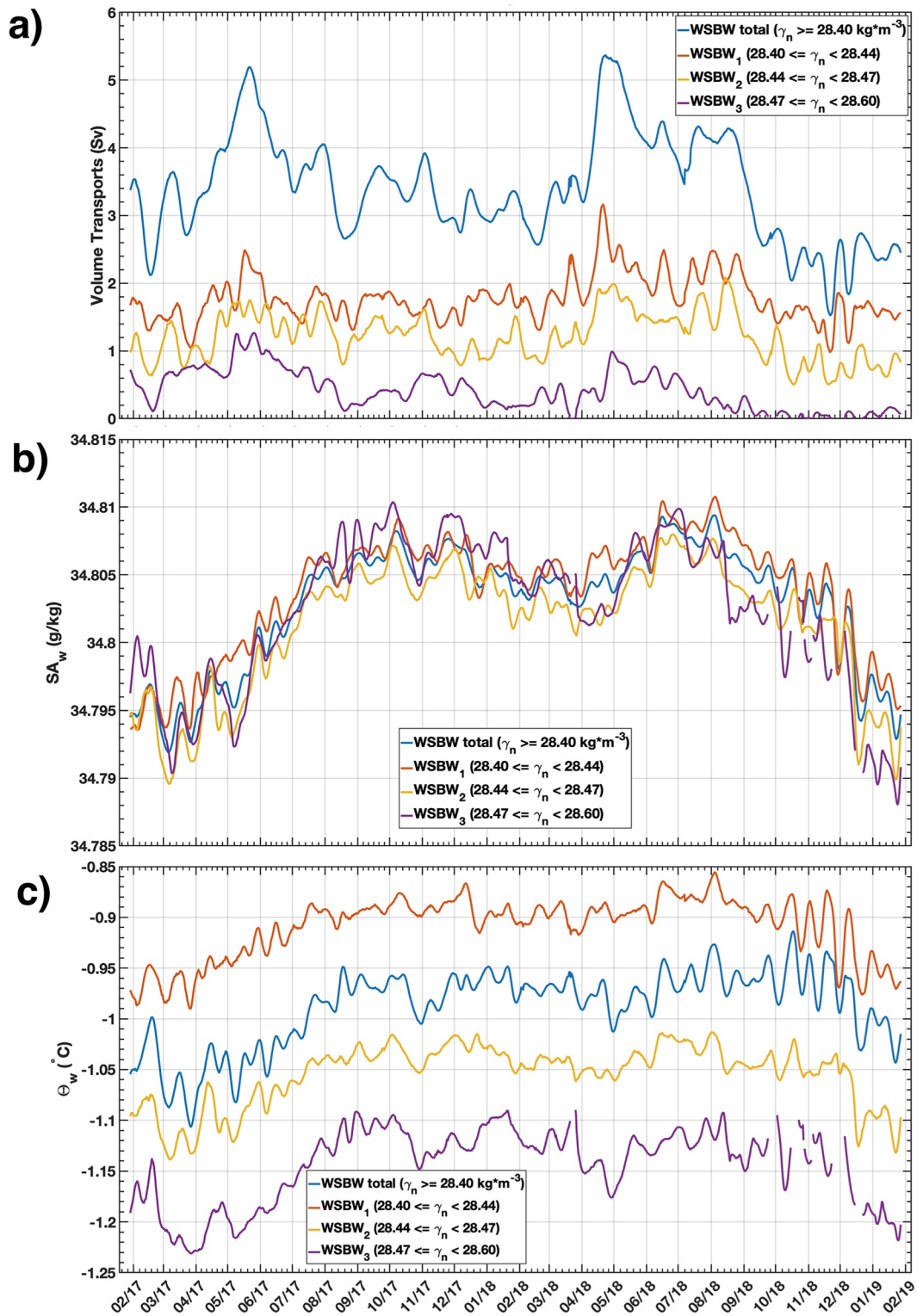

Figure 9. Time series of the total Weddell Sea Bottom Water (WSBW) (blue line) and the 3 different WSBW density subclasses for (a) Volume transports (Sv) and the transport-weighted (b) absolute salinity (SA_w, in g/kg) and (c) conservative temperature (Θ_w, in ºC).

21699291, 2023, 2, Downloaded from https://agupubs.onlinelibrary.wiley.com/doi/10.1029/2022JC019375 by Wiley, Wiley Online Library on [14/02/2023]. See the Terms and Conditions (https://onlinelibrary.wiley.com/terms-and-conditions) on Wiley Online Library for rules of use; OA articles are governed by the applicable Creative Commons License

5. Discussion

5.1. On the WSBW Annual-Mean Properties

Here we compare our results, for a Θ boundary, with previous studies that used a θ boundary to delimit the WSBW plume. The annual-mean cross-section area estimated from our highly instrumented mooring array (~45 km^2) is within the observed range (37–56 km^2) derived from 5 full-depth CTD surveys of the same transect, sampled between 1989 and 1998 and covering all seasons except winter (Fahrbach et al., 2001). In addition, our annual-mean transport estimate (4.7 ± 1.1 Sv) agrees considerably well with previous studies using either inverse models (4.5 ± 0.9 Sv, for data collected in April 1999, Naveira Garabato et al., 2002), moored current-meters deployed between 1968 and 1999 (4.3 ± 1.4 Sv, Foldvik et al., 2004) or hydrographic transects sampled in February 1973 (3.6 Sv, Foster and Carmack, 1976). However, our estimated annual-mean WSBW transport is considerably larger than an earlier estimate for this transect (1.3 ± 0.2 Sv, Fahrbach et al., 2001), which was derived from an historical mooring record with lower spatial resolution, covering from 1989 to 1997, and with some time gaps in between. For comparison, we computed the annual-mean WSBW transport considering the same longitudinal range as in Fahrbach et al. (2001), but using our higher spatial resolution mooring array, and we obtained a WSBW transport of 3.55 Sv for a Θ boundary. This discrepancy can be explained by the fact that they did not have a mooring located at the position of our NW2 mooring, where the strongest velocity core is found (see Figure 7 in Fahrbach et al. (2001)).

5.2. On the WSBW Seasonal Variability

The fluctuations found at seasonal timescales in WSBW transports may either be caused by changes in the volume of dense precursors exported further upstream, by changes in the strength of the Weddell Gyre imposed by the curl of the winds, or by a combination of both (Fahrbach et al., 2001; Gordon et al., 2010; le Paih et al., 2020). In this regard, the anticorrelation that we observed in November between the change in WSBW area and velocity suggests a seasonal weakening of the wind-driven component of the WSBW flow (i.e., a weakening of the Weddell Gyre), as this decrease in WSBW velocity would increase its cross-section area (Fahrbach et al., 2001). On the other hand, the synchronous decrease of WSBW area and velocity in February indicates a seasonal decrease in the rate of WSBW formation taking place earlier in its source regions further upstream (Fahrbach et al., 1995, 2001). The seasonal variability of the WSBW properties described here is similar in magnitude to the variability previously described for the NW Weddell Sea (Fahrbach et al., 2001). Schröder et al. (2002) compared the WSBW properties in the same transect, but occupied in April 1998 and January 2000. They found that the WSBW plume was clearly warmer and thinner in January 2000 compared to April 1998. This is in good agreement with the seasonal cycle of WSBW described in our study.

The seasonal minimum in WSBW salinity that we observed during the austral summer likely results from the entrainment of a larger fraction of freshwater originating from summer sea ice melt. In fact, the summer relaxation of the southerly winds along the eastern side of the Antarctic Peninsula (Gordon et al., 2010) would allow more freshwater to reach the shelf break region where it could be entrained by the dense plumes of WSBW precursors cascading down-slope.

5.3. On the WSBW Varieties Transported by the Velocity Cores

The first velocity core, located at NW2, is fresher and shallower than the other two velocity cores, which indicates that the WSBW variety transported within this core contains a larger fraction of the less saline shelf waters characteristic of nearby sources such as the Larsen Ice Shelf region (compared to the more saline shelf waters usually found in the southern Weddell Sea). This would agree with previous studies that indicated the existence of a WSBW source region in the western Weddell Sea (Absy et al., 2008; Anderson et al., 1991; Fahrbach et al., 1995; Gordon et al., 1993; Muench & Gordon, 1995; van Caspel et al., 2015). The second velocity core, centered at NW4, presents lower velocities but it transports the densest, coldest and saltiest variety of WSBW (Figures 7 and 8). This is likely the same velocity core that was previously found by Muench and Gordon (1995) between 2,000 and 2,500 m depth in several cross-slope sections obtained further south in the western Weddell Sea. Moreover, the high salinities found in the second core suggest the presence of remnants of the WSBW formed in the Filchner-Ronne Ice Shelf area in the southern Weddell Sea (Fahrbach et al., 1995; Foldvik et al., 2004). Furthermore, in a different cross-slope transect obtained further upstream at about 65°S, van Caspel et al. (2015)

21699291, 2023, 2, Downloaded from https://agupubs.onlinelibrary.wiley.com/doi/10.1029/2022JC019375 by Wiley, Wiley Online Library on [14/02/2023]. See the Terms and Conditions (https://onlinelibrary.wiley.com/terms-and-conditions) on Wiley Online Library for rules of use; OA articles are governed by the applicable Creative Commons License

identified a WSBW core with high dissolved oxygen values at roughly the same depth range (2,800 m) as our second velocity core. They concluded that the observed increase in oxygen at such depths could be explained by the presence of a WSBW plume exported in the Filchner-Ronne region. The third velocity core, centered at NW6, is only discernible when the second velocity core weakens and retreats upslope. Its velocity is maximum in December and minimum in September (Figure 8). Thus, its maximum speed is reached with a 7 month-delay compared to the other two velocity cores. This delay is probably caused by its weaker velocities. The second and third velocity cores transport a saltier WSBW variety, likely originated in the southern Weddell Sea. In fact, they probably correspond to the two plumes of dense waters flowing westward along the slope identified by Foldvik et al. (2004) just west of the Filchner Trough (see their Figure 1b). The first and second velocity cores are clearly denser, colder and saltier when their speed is maximum compared to when their speed is minimum (Figure 8). In contrast, the third velocity core is warmer and fresher at high-flow events. This pattern was also detected by the transport composite analysis and is likely the result of a larger WDW influence on the third velocity core given its deeper location in the interior of the Gyre.

The three velocity cores described here were also detected in the LADCP section occupied in February 2007 during the *Antarctic Drifter Experiment*: *Links to Isobaths and Ecosystem* project (Thompson and Heywood, 2008, hereafter TH2008). They indicated that the northward flow characteristic of the Antarctic Slope Front (ASF) was associated with two velocity cores. Our first velocity core is probably the same core as the seaward bottom velocity core of the ASF observed by TH2008. Interestingly, our first core presents a mean velocity in February (Figure 7c) that is 25% higher than the velocity found in their core (Figure 9 in TH2008). Since our first core is highly baroclinic, it is not clear whether it is linked to the shoreward core of the ASF, which was clearly barotropic in TH2008. We did not observe this barotropic core in our mooring array, probably because of a lower spatial resolution compared to the LADCP survey used in TH2008. Interestingly, the shoreward core of the ASF is actually present in the data from an older mooring (AWI-206), which was deployed near the 900 m isobath (Fahrbach et al., 2001). However, Fahrbach et al. (2001) found weaker annual mean velocities and they did not observe the barotropic flow found in TH2008. On the other hand, our second velocity core is located within the upper part of the Weddell Front described in TH2008, while our third core would correspond to the weaker core of northward velocity found between 3,400 and 4,000 m depth in TH2008. This deeper and weaker core was also detected by Fahrbach et al. (1995, 2001).

5.4. Large-Scale Drivers of WSBW Interannual Variability

In what follows, we discuss the plausible drivers behind the decrease in the densest WSBW subclass, along with the coincident increase in the lighter WSBW subclasses, observed during the AMJ 2018 period compared to AMJ 2017. This situation might either be explained by a decrease in the density of the dense WSBW precursors (i.e., ISW, HSSW), which are exported down-slope in its source regions (first hypothesis), or by warmer and slightly saltier ambient waters (i.e., a less modified WDW) being entrained by these dense precursors when cascading downslope (second hypothesis). The export of dense WSBW precursors to the shelf-break takes place mainly along the Filchner Trough in the southern Weddell Sea (Carmack & Foster, 1975a; Foldvik et al., 2004; Nicholls & Østerhus, 2004), but also in front of the Larsen Ice Shelf in the western Weddell Sea (Absy et al., 2008; Anderson et al., 1991; Fahrbach et al., 1995; Huhn et al., 2008; Hutchinson et al., 2020; Muench & Gordon, 1995; van Caspel et al., 2015). Previous studies identified two types of ISW cascading down the Filchner sill into the continental slope (Akhoudas et al., 2020; Janout et al., 2021; Nicholls & Østerhus, 2004). The first type is a local variety of ISW (Berkner-sourced ISW), while the second ISW type originates from the Ronne HSSW, which is further transformed along its pathway inside the Ronne Ice Shelf cavity toward the Filchner Trough. Due to its longer interaction with the shelf ice, the Ronne-sourced ISW is slightly fresher, although still slightly denser than the Berkner-sourced ISW (Janout et al., 2021). Recent hydrographic data from the southern Weddell Sea, from two oceanographic cruises (Akhoudas et al., 2020; Janout et al., 2021) and from drill hole moorings below the Filchner ice shelf (Hattermann et al., 2021), indicate a transition in mid-2017 from a Berkner-sourced ISW to a Ronne-sourced ISW dominance in Filchner Trough. If we assume the same entrainment efficiency of ambient waters by both types of ISW given their nearly similar densities (Janout et al., 2021), this transition to a Ronne-sourced ISW would imply a slightly denser but fresher WSBW arriving at our northwest Weddell Sea moorings in the AMJ 2018 period. However, we observed a ~30% reduction of the densest WSBW subclass during this period. This suggests that the first hypothesis might not be correct, at least when considering the

21699291, 2023, 2, Downloaded from https://agupubs.onlinelibrary.wiley.com/doi/10.1029/2022JC019375 by Wiley, Wiley Online Library on [14/02/2023]. See the Terms and Conditions (https://onlinelibrary.wiley.com/terms-and-conditions) on Wiley Online Library for rules of use; OA articles are governed by the applicable Creative Commons License

WSBW sourced from the Filchner Through, which is the most probable source region for the densest variety of WSBW. Note that, after Gordon et al. (2010), we estimate that a WSBW plume sourced in front of the Filchner Trough should arrive at our moorings after 4–6 months.

Given the lack of data from the Larsen C source region between 2016 and 2018, we cannot rule out that possible changes in the export of dense WSBW precursors from this region are behind the observed decrease in the densest WSBW subclass. In this regard, van Caspel et al. (2015) used data collected during the "Ice Station POLarstern" (ISPOL) drift experiment (Hellmer et al., 2008) to describe the characteristic thermohaline properties of the dense waters found in front of Larsen C Ice Shelf (see their Table 2). Then, assuming that the interannual variability of the dense precursors of WSBW is well represented by the standard deviations described by van Caspel et al. (2015), and if we assume a Gaussian normal distribution of their themohaline values, this would imply that 95% of the data points would be contained between a temperature anomaly of ±0.002°C and a salinity anomaly of ±0.018 psu from their respective means (i.e., mean ± 2*std). However, the temperature anomaly we observed in the densest WSBW subclass was an order of magnitude larger (+0.04°C). This suggests that the first hypothesis might not hold either for the source region in front of Larsen C Ice Shelf. Nevertheless, this should be regarded with caution given the scarcity of data.

To further assess the second hypothesis, that is, the entrainment of a less modified WDW, we analyzed the change in thermohaline properties of WSBW between the two annual transport peaks that occurred on 23 April 2018 (A18) and 21 May 2017 (M17) respectively. We found that the three WSBW density subclasses were warmer and slightly saltier during the A18 peak, especially the less dense WSBW subclass, which presented the largest positive anomalies in Θ and SA (Section 4.5). This suggests warmer and slightly more saline ambient waters (i.e., a less modified WDW) being entrained in early 2018, as this would have a stronger effect on the properties of the less dense WSBW subclass, given that it occupies the outer layer of the WSBW.

In this regard, it is well accepted that positive SAM-periods induce poleward migration of the westerly wind belt in the Southern Hemisphere (Thompson & Solomon, 2003) and a weakening of the northward winds, or even southward winds, in the eastern side of the Antarctic Peninsula (Lefebvre et al., 2004; McKee et al., 2011). This wind shift decreases the onshore oceanic Ekman transport, weakening the slope of the thermocline in the ASF and enabling warm subsurface waters to reach shallower depths in the vicinity of the Antarctic continental shelf break (Spence et al., 2014). Furthermore, in a recent model intercomparison analysis with 22 CMIP6 models, the temperature of shelf bottom waters around Antarctica was found to be significantly correlated with the SAM, with a positive SAM corresponding to warmer shelf waters (Purich and England, 2021). In the specific case of the southern Weddell Sea, several months with positive SAM values would also imply a poleward displacement of the WDW upwelling region and the arrival of less modified (i.e., warmer and saltier) WDW in the vicinity of the shelf break, where it could be entrained by the dense precursors of WSBW when cascading downslope (Figure 10). Employing mooring data from the shelf break north of Filchner Trough, Årthun et al. (2012) observed a shoaling of the thermocline and thus a larger presence of WDW at the shelf break, likely enabled by the seasonal weakening of along-shore winds during March. In fact, the wind-induced shoaling of the thermocline in the ASF has been observed to be relevant for the shelf-basin exchange in this area (Ryan et al., 2017). Given that in the southern Weddell Sea a positive SAM weakens the easterlies blowing along the Antarctic margins (Figure 10), a larger presence of WDW is to be expected at the shelf break during these events (Darelius et al., 2016). In the case of the northwestern Weddell Sea, the weakening of the southerlies in the eastern side of the Antarctic Peninsula induced by a positive SAM would also enhance the presence of a less modified WDW near the shelf break. In this regard, the observation-based SAM Index (Marshall, 2003) was markedly negative between November 2016 (−3.12) and March 2017 (−1.56), while it was markedly positive between November 2017 (3.18) and February 2018 (1.02). This is reflected in ERA5 wind reanalysis data (Hersbach et al., 2020) by weaker easterlies in the southern Weddell Sea and weaker southerlies in the western Weddell Sea between November 2017 and February 2018 compared to the same period in the previous year (Figure S3 in Supporting Information S1). This supports the hypothesis of a less modified WDW being entrained during the formation of WSBW (Figure 10) and, consequently, the warmer, slightly saltier and less dense WSBW arriving at our moorings in April 2018, after a time lag of 4–6 months from its formation regions.

To further investigate the second hypothesis, we constructed a historical time series (2005–2022) with the bottom thermohaline properties measured at mooring NW3 (see Section 3). We then smoothed the NW3 thermohaline record and SAM index with a 3-month running-mean window and performed a lagged cross-correlation anal-

21699291, 2023, 2, Downloaded from https://agupubs.onlinelibrary.wiley.com/doi/10.1029/2022JC019375 by Wiley, Wiley Online Library on [14/02/2023]. See the Terms and Conditions (https://onlinelibrary.wiley.com/terms-and-conditions) on Wiley Online Library for rules of use; OA articles are governed by the applicable Creative Commons License

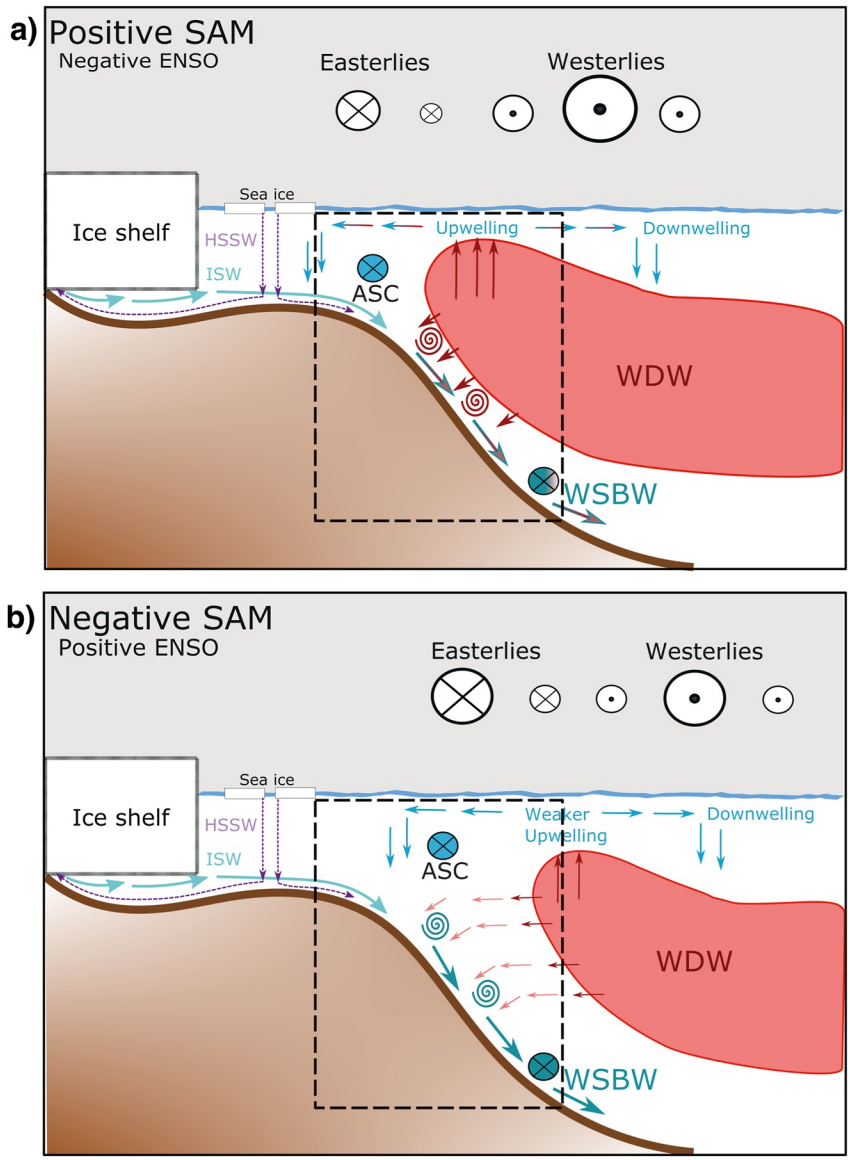

Figure 10. Schematic showing the contrasting wind field and ocean setting for the Southern Weddell Sea between: (a) A positive Southern Annular Mode (SAM) occurring with a negative El Niño-Southern Oscillation (ENSO); and (b) A negative SAM occurring with a positive ENSO. WSBW: Weddell Sea Bottom Water; WDW: Warm Deep Water; HSSW: High Salinity Shelf water; ISW: Ice Shelf Water; ASC: Antarctic Slope Current. The dashed rectangle highlights the change in the ambient waters entrained by the descending plumes and their influence on the Weddell Sea Bottom Water properties between both cases.

ysis between these time series with a 24 months lead/lag time period considered. We found that the Θ measured at NW3 is positively correlated ($r = 0.29$, $p < 0.05$) with the SAM phase occurring 5.5 months before (Figure S4 in Supporting Information S1). Thus, a positive SAM would be related to a warmer WSBW being subsequently observed at our moorings, in agreement with our second hypothesis. This result agrees well with McKee et al. (2011), who also found a significant positive correlation between SAM and the Θ of the WSBW reaching 9 months later to their M3 mooring (see their Figure 4), located roughly 400 km further downstream in the southern slope of the South Orkney Plateau. However, they focused their discussion on the cooling of WSBW that they found between 1 and 6 months after a positive SAM (see their mechanism II) and on the warming of WSBW occurring with a time lag of 14–18 months after a positive SAM (see their mechanism I). On the other hand, previous studies have suggested that ENSO can also influence the winds, sea ice and hydrographic properties in different Antarctic regions (Barnes et al., 2006; Dotto et al., 2016; Gordon et al., 2020; Meijers et al., 2016;

21699291, 2023, 2, Downloaded from https://agupubs.onlinelibrary.wiley.com/doi/10.1029/2022JC019375 by Wiley, Wiley Online Library on [14/02/2023]. See the Terms and Conditions (https://onlinelibrary.wiley.com/terms-and-conditions) on Wiley Online Library for rules of use; OA articles are governed by the applicable Creative Commons License

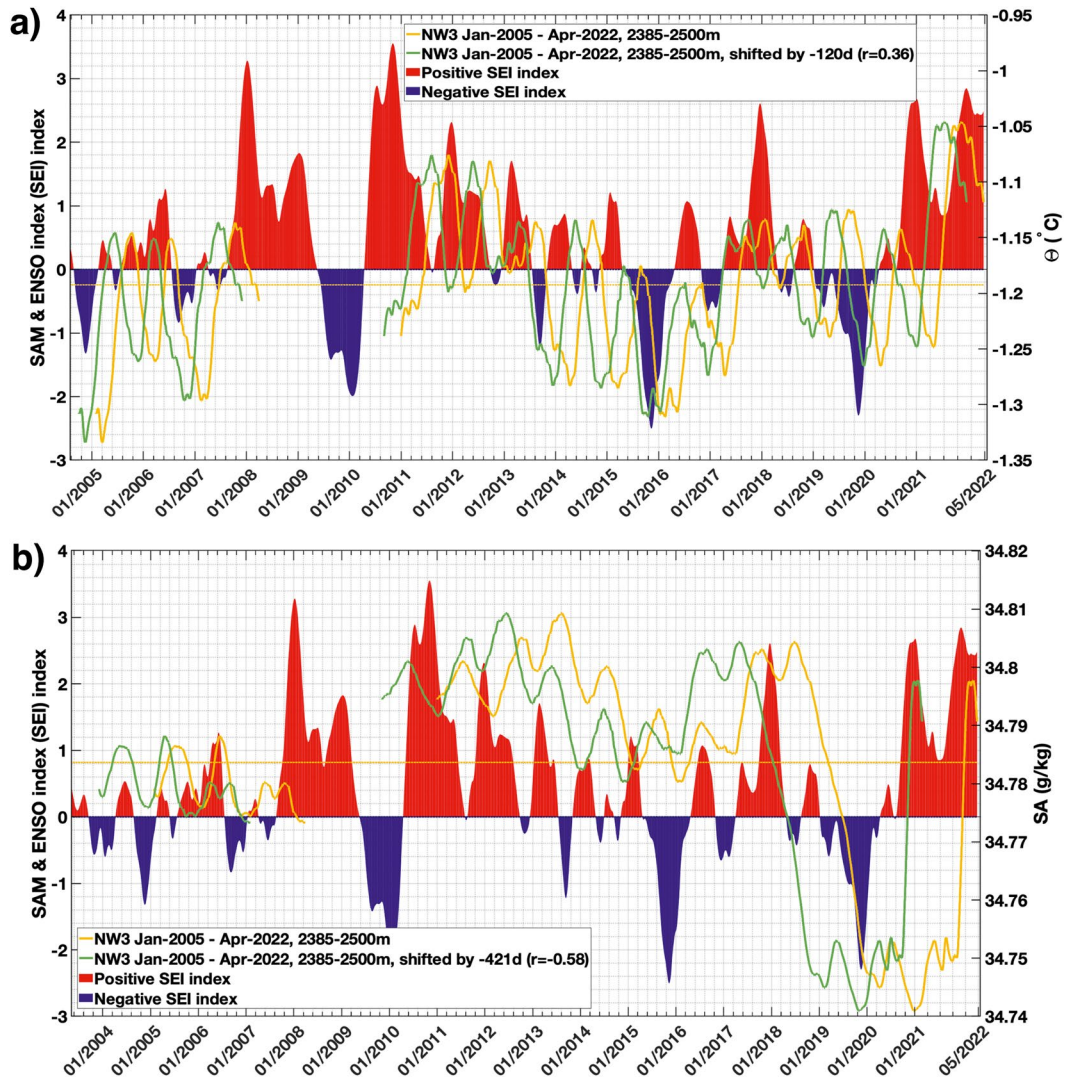

Figure 11. (a) Time series of the SAM-ENSO index (SEI, blue and red patches), the conservative temperature (Θ, °C) for the historical NW3 time series at 2,385–2,500 m (yellow line), and the same NW3 time series shifted (green line) by the lag (−120 days) corresponding to its maximum significant cross-correlation ($r = 0.36$, $p < 0.05$) with the SEI time series. The Θ mean of the time series is also shown (horizontal yellow line). (b) Time series of the SEI (blue and red patches), the absolute salinity (S_A, g/kg) for the historical NW3 time series at 2,385–2,500 m (yellow line), and the same NW3 time series shifted (green line) by the lag (−421 days) corresponding to its maximum significant cross-correlation ($r = -0.58$, $p < 0.05$) with the SEI time series. The SA mean of the time series is also shown (horizontal yellow line). All the time series have been previously smoothed with a 3-month running-mean.

Meredith et al., 2004; Yuan, 2004). Particularly, a positive ENSO induces positive anomalies in the meridional wind in the eastern side of the Antarctic Peninsula (i.e., stronger southerlies) and the opposite occurs during a negative ENSO (McKee et al., 2011; Yuan, 2004). The effects induced on the winds around Antarctica by ENSO and SAM are reinforced when they occur in opposite phases (i.e., a positive SAM with a *La Niña* or a negative SAM with an *El Niño*), while the SAM forcing is partially compensated when they occur at the same phase (Fogt et al., 2011; Gordon et al., 2010; Jullion et al., 2010; Martinson & Iannuzzi, 2003; McKee et al., 2011; Stammerjohn et al., 2008). Therefore, we constructed a new climate index (SEI) in order to account for the combined effects of SAM and ENSO on the winds (see Section 3). Using the SEI time series the correlation with the Θ measured at NW3 further increased ($r = 0.36$, $p < 0.05$), while the time lag decreased to 4 months (Figure 11a). This higher correlation underlines the benefits of considering both SAM and ENSO states to explain the Θ changes observed in the WSBW reaching the NW Weddell Sea.

21699291, 2023, 2, Downloaded from https://agupubs.onlinelibrary.wiley.com/doi/10.1029/2022JC019375 by Wiley, Wiley Online Library on [14/02/2023]. See the Terms and Conditions (https://onlinelibrary.wiley.com/terms-and-conditions) on Wiley Online Library for rules of use; OA articles are governed by the applicable Creative Commons License

In contrast to the Θ case, our lagged cross-correlation analysis between SA and SAM was unable to explain the slight increase in salinity that we measured in AMJ 2018. In fact, we found that the SA at NW3 is anticorrelated ($r = -0.22$, $p < 0.05$) with the SAM state occurring 13 months earlier. This means that a positive SAM would induce a fresher WSBW measured in our moorings after more than 1 year (Figure S5 in Supporting Information S1). We propose that this WSBW freshening is caused by the same mechanism that induces the WSBW warming at the M3 mooring 14–18 months after a positive SAM, that is, the mechanism I described by McKee et al. (2011). This mechanism consists in meridional wind anomalies in the eastern side of the Antarctic Peninsula during the summer driving the sea ice concentration in the southwestern Weddell Sea and thus, conditioning the area of surface ocean exposed during the next winter and the amount of HSSW formed due to brine rejection from new sea ice. Note that both a positive SAM and a *La Niña* event in summer would induce negative meridional wind anomalies (i.e., weaker southerlies) in the eastern side of the Antarctic Peninsula (Figure S3 in Supporting Information S1) and thus, an increase in the sea ice concentration in the southwestern Weddell Sea. This implies a decrease in the HSSW formed in winter that year. This reduced replenishment of dense shelf waters would result in the export of fresher and warmer WSBW precursors downslope during the next austral summer. In this regard, the magnitude of the anticorrelation with SA increases ($r = -0.58$, $p < 0.05$) when using the SEI index instead of SAM, while the time lag slightly increases to 13.8 months (Figure 11b). This is reasonable, as the meridional wind anomalies in the eastern side of the Antarctic peninsula are strongly influenced by the ENSO phase (Fogt et al., 2011; Yuan, 2004). In fact, we found a quite strong positive correlation ($r = 0.52$, $p < 0.05$) between ENSO and the SA of WSBW measured 15 months later at mooring NW3 (not shown). An additional freshening mechanism was proposed by Gordon et al. (2020). They observed that a positive SAM usually induces a more cyclonic wind curl in the Weddell Sea and suggested that this would induce the freshening of the WSBW measured 18 months later at the southern slopes of the Orkney Plateau. Specifically, they proposed that the intensification of the Weddell Gyre would deepen the V-shaped double front found above the shelf break in the western Weddell Sea (see their Figure 3b). Then, the thermobaric effect would promote further descent of the relatively fresh waters within the V-shaped trough, enabling them to mix with the WSBW layer. Both McKee's and Gordon's mechanisms might be related to the extended period of WSBW freshening that we observed later, from September 2018 until at least the end of January 2019, when our moorings were recovered. In fact, the recently extended record at mooring NW3 shows that this freshening lasted until December 2021 at mooring NW3 (yellow line in Figure 11b).

On the other hand, we observed a marked reduction in WSBW transport, cross-section area and density between September 2018 and the end of January 2019, compared to the previous year. This synchronous reduction was probably caused by a decrease in the export of the dense precursors of WSBW during the austral autumn of 2018. However, the observed WSBW density decrease was roughly coincident with the marked freshening of the WSBW plume. This suggests that the freshening mechanisms discussed above also played a role in the observed WSBW density reduction.

On top of the wind forcing, a freshening of the surface shelf waters could also enhance the presence of WDW at the shelf break by means of increased baroclinic instability (Hattermann, 2018). This can occur due to increased ice shelf basal melting (Hattermann, 2018) or by fresh-water advection from upstream regions like the Dronning Maud Land coast (Ryan et al., 2020).

6. Summary and Conclusions

We have investigated the annual-mean, seasonal cycle and interannual variability of the transports and properties of the WSBW plume. For this purpose, we analyzed a densely instrumented mooring array deployed between 2017 and 2019 across the continental slope of the NW Weddell Sea. We found that the annual-mean WSBW transport is 3.4 ± 1.5 Sv, with a cross-section area of ~35 km^2 and a maximum thickness of 203 m (for a γ_n boundary). These values are larger when using a Θ boundary to delimit the WSBW (4.7 ± 1.1 Sv, ~45 km^2 and 232 m). On the other hand, the annual-mean transport-weighted properties of WSBW are −0.99°C, 34.803 g/kg and 28.44 kg/m^3 (for a γ_n boundary), while the WSBW is slightly colder, fresher and less dense when defined by a Θ boundary.

The WSBW presents three bottom-intensified velocity cores that vary in intensity along their seasonal cycle. The first core is located at the 1,660 m isobath and is the freshest and fastest flowing of the three. The second core is located near the 2,760 m isobath, it has weaker velocities yet carries the densest WSBW variety, while the third

21699291, 2023, 2, Downloaded from https://agupubs.onlinelibrary.wiley.com/doi/10.1029/2022JC019375 by Wiley, Wiley Online Library on [14/02/2023]. See the Terms and Conditions (https://onlinelibrary.wiley.com/terms-and-conditions) on Wiley Online Library for rules of use; OA articles are governed by the applicable Creative Commons License

velocity core is the weakest, warmest and deepest (3.880 m isobath). The first core transports a high fraction of a WSBW variety likely originated in the Larsen Ice Shelf region, while the second and third cores transport more saline WSBW varieties that were likely sourced further upstream in the southern Weddell Sea.

The seasonal peak of WSBW transport and cross-section area is reached in May (4.65 Sv, 37.9 km^2). After May, WSBW transports and areas decrease progressively until reaching their minimum in February (2.80 Sv, 33.4 km^2). However, the exact timing of the maximum and minimum values can shift slightly from year to year. The coldest and densest WSBW is measured in May, indicating the arrival of the pulse of newly formed WSBW to the NW Weddell Sea.

Between April and June 2018, the WSBW plume was less dense, warmer and slightly saltier than during the same period in 2017. These changes can be explained by the entrainment of a less modified WDW at the shelf break during the formation of WSBW further upstream in 2018, compared to 2017. We propose that this was enabled by the weakening of the along-shore winds induced by the combined effect of a positive SAM and a cold phase of ENSO taking place between November 2017 and February 2018. Weaker along-shore winds result in the lifting of the thermocline and thus enable the presence of a less modified WDW in the vicinity of the shelf break. To further investigate this, we created a combined SAM-ENSO climate index and performed a lagged cross-correlation analysis with a 2005–2022 timeseries of WSBW properties at mooring NW3. Our results indicate that a positive SAM, reinforced by a cold phase of ENSO, can influence the WSBW properties measured in the NW Weddell Sea at two different time scales. First, it would produce a warmer and slightly saltier WSBW that would reach our moorings with a time delay between 4 and 5 months. This change in WSBW properties can be explained by the mechanism proposed here (i.e., the entrainment of a less modified WDW during the formation of WSBW). Second, it would induce a WSBW freshening that would be observed in the NW Weddell Sea after 13–14 months. This freshening is likely related with these two SAM-induced freshening mechanisms: (a) A reduced HSSW formation and subsequent export driven by negative anomalies in meridional winds in the eastern side of the Antarctic Peninsula during the previous summer (McKee et al., 2011), and (b) the injection of fresh shelf waters into the WSBW layer via a wind-driven deepening of the V-shaped double front located at the shelf break in the western Weddell Sea (Gordon et al., 2020).

Between September 2018 and the end of January 2019, we observed a synchronous reduction in WSBW transport, cross-section area and density, compared to the previous year. This reduction likely resulted from a decrease in the volume of WSBW formed during the austral autumn of 2018, although the SAM-induced freshening of WSBW may have also contributed.

Our results underline the importance of long time series for ocean and climate research in order to understand local and large-scale processes and to detect changes. Among many aspects, the Weddell Sea is a key region for dense water formation and thus it is directly relevant for the global ocean circulation and the Earth's climate. The continuation of these relevant time series into the future would allow to advance our understanding and reduce model uncertainties associated to the future evolution of the Earth system.

Data Availability Statement

The 2017–2019 mooring data set (Rohardt & Boebel, 2019a, 2019b, 2019c, 2019d, 2019e, 2019f, 2019g) and the historical data of mooring NW3 (Fahrbach & Rohardt, 2012; Rohardt & Boebel, 2017, 2019e) is available in Pangaea (https://www.pangaea.de/) with the Pangaea codes displayed in Table S1 and Table S2 in Supporting Information S1. The SAM index values were obtained from Marshall (2003), available at https://legacy.bas.ac.uk/met/gjma/sam.html. The Oceanic Niño Index (ONI) is provided by the NOAA Climate Prediction Center in the following web page https://origin.cpc.ncep.noaa.gov/products/analysis_monitoring/ensostuff/ONI_v5.php. The SAM-ENSO index (SEI) employed here is now available from Llanillo et al. (2023) at https://doi.org/10.5281/zenodo.7500163. The deployment (PS103) and recovery (PS117) cruise reports (Boebel, 2017, 2019) are also available online at (https://epic.awi.de/id/eprint/45596/1/BzPM_0710_2017.pdf, and https://epic.awi.de/id/eprint/49913/1/BzPM_0732_2019.pdf). The cruise reports related to the long-term thermohaline time series employed here (PS129_06, (PS103_1), ANT-XXVII_2 and ANT-XXII_3) are available at https://epic.awi.de/id/eprint/55571/1/Expeditionsprogramm_PS129.pdf, https://epic.awi.de/id/eprint/26708/1/BerPolarforsch2006533.pdf and https://cchdo.ucsd.edu/data/7125/ANT%20XXVII-2-final-klein%20cruise%20report.pdf (Fahrbach, 2005, 2011; Hoppema, 2022).

21699291, 2023, 2, Downloaded from https://agupubs.onlinelibrary.wiley.com/doi/10.1029/2022JC019375 by Wiley, Wiley Online Library on [14/02/2023]. See the Terms and Conditions (https://onlinelibrary.wiley.com/terms-and-conditions) on Wiley Online Library for rules of use; OA articles are governed by the applicable Creative Commons License

Acknowledgments
This study used data provided by the Alfred Wegener Institute - Helmholtz Center for Polar and Marine Research in Bremerhaven (Grants ANT-XXII_3, ANT-XXVII_2, AWI-PS103_01, AWI-PS117_01 and AWI-PS129_06). The authors thank the scientists and technicians that collected the employed data sets, together with the support provided by the captains and crews of *RV Polarstern* (AWI, 2017). We would also like to thank our colleagues from the Southern Ocean Carbon and Heat Impact on Climate (SO-CHIC) project and H. Hellmer for their scientific input and two anonymous reviewers for their insightful comments that helped to improve this manuscript. This project received funding from the EU's Horizon 2020 Research and Innovation Program under the Grant agreement No. 821001 (SO-CHIC), and therein is a contribution to its Work Package 3. This study is further a contribution to the project T3 of the Collaborative Research Centre TRR 181 "Energy Transfers in Atmosphere and Ocean" funded by the Deutsche Forschungsgemeinschaft (DFG, German Research Foundation; project no. 274762653). Open Access funding enabled and organized by Projekt DEAL.

References

Abrahamsen, E. P., Meijers, A. J. S., Polzin, K. L., Naveira Garabato, A. C., King, B. A., Firing, Y. L., et al. (2019). Stabilization of dense Antarctic water supply to the Atlantic Ocean overturning circulation. *Nature Climate Change*, *9*(10), 742–746. https://doi.org/10.1038/s41558-019-0561-2

Absy, J. M., Schröder, M., Muench, R., & Hellmer, H. H. (2008). Early summer thermohaline characteristics and mixing in the western Weddell Sea. *Deep-Sea Research Part II Topical Studies in Oceanography*, *55*(8–9), 1117–1131. https://doi.org/10.1016/j.dsr2.2007.12.023

Akhoudas, C., Sallée, J. B., Reverdin, G., Aloisi, G., Benetti, M., Vignes, L., & Gelado, M. (2020). Ice shelf basal melt and influence on dense water outflow in the southern Weddell Sea. *Journal of Geophysical Research: Oceans*, *125*(2), 1–19. https://doi.org/10.1029/2019JC015710

Anderson, L. G., Holby, O., Lindegren, R., & Ohlson, M. (1991). The transport of anthropogenic carbon dioxide into the Weddell Sea. *Journal of Geophysical Research*, *96*(C9), 16679. https://doi.org/10.1029/91jc01785

Årthun, M., Nicholls, K. W., Makinson, K., Fedak, M. A., & Boehme, L. (2012). Seasonal inflow of warm water onto the southern Weddell Sea continental shelf, Antarctica. *Geophysical Research Letters*, *39*(17), 2–7. https://doi.org/10.1029/2012GL052856

Bamston, A. G., Chelliah, M., & Goldenberg, S. B. (1997). Documentation of a highly ENSO-related SST region in the equatorial Pacific: Research note. *Atmosphere-Ocean*, *35*(3), 367–383. https://doi.org/10.1080/07055900.1997.9649597

Barnes, D. K. A., Fuentes, V., Clarke, A., Schloss, I. R., & Wallace, M. I. (2006). Spatial and temporal variation in shallow seawater temperatures around Antarctica. *Deep–Sea Research II*, *53*(8–10), 853–865. https://doi.org/10.1016/j.dsr2.2006.03.008

Boebel, O. (2017). The expedition PS103 of the research vessel POLARSTERN to the Weddell Sea in 2016/2017. In *Berichte zur Polar-und Meeresforschung=Reports on polar and marine research (version 1.0)*. Alfred-Wegener-Institut, Helmholtz-Zentrum für Polar-und Meeresforschung. https://doi.org/10.2312/BZPM_0710_2017

Boebel, O. (2019). The expedition PS117 of the research vessel POLARSTERN to the Weddell Sea in 2018/2019. In *Berichte zur Polar-und Meeresforschung=Reports on polar and marine research (version 1.0)*. Alfred-Wegener-Institut, Helmholtz-Zentrum für Polar- und Meeresforschung. https://doi.org/10.2312/BZPM_0732_2019

Carmack, E. C., & Foster, T. D. (1975a). Circulation and distribution of oceanographic properties near the Filchner Ice Shelf. *Deep-Sea Research and Oceanographic Abstracts*, *22*(2), 77–90. https://doi.org/10.1016/0011-7471(75)90097-2

Carmack, E. C., & Foster, T. D. (1975b). *On the flow of water out of the Weddell Sea* (Vol. 22). P©rgamon Press.

Darelius, E., Fer, I., & Nicholls, K. W. (2016). Observed vulnerability of Filchner-Ronne Ice Shelf to wind-driven inflow of warm deep water. *Nature Communications*, *7*, 1–7. https://doi.org/10.1038/ncomms12300

de Carvalho Ferreira, M. L., & Kerr, R. (2017). Source water distribution and quantification of North Atlantic deep water and Antarctic bottom water in the Atlantic Ocean. *Progress in Oceanography*, *153*, 66–83. https://doi.org/10.1016/j.pocean.2017.04.003

Dotto, T. S., Kerr, R., Mata, M. M., & Garcia, C. A. E. (2016). Multidecadal freshening and lightening in the deep waters of the Bransfield Strait, Antarctica. *Journal of Geophysical Research: Oceans*, *121*, 1–38. https://doi.org/10.1002/2015JC011228

Fahrbach, E. (2005). *Weekly report for R.V. Polarstern expedition ANT-XXII/3, report no. 1 (30.01.2005), English version*. Alfred-Wegener-Institute for Polar-and Marine Research, Bremerhaven, Bremerhaven, Alfred Wegener Institute for Polar and Marine Research. hdl:10013/epic.27210.

Fahrbach, E. (2011). The expedition of the research vessel Polarstern to the Antarctic in 2010/11 (ANT-XXVII/2). In *Berichte zur Polar-und Meeresforschung=Reports on polar and marine research (version 1.0)*. Alfred-Wegener-Institut für Polar-und Meeresforschung. https://doi.org/10.2312/BZPM_0634_2011

Fahrbach, E., Harms, S., Rohardt, G., Schröder, M., & Woodgate, A. R. (2001). Flow of bottom water in the northwestern Weddell Sea. *Journal of Geophysical Research*, *106*(C2), 2761–2778. https://doi.org/10.1029/2000jc900142

Fahrbach, E., Hoppema, M., Rohardt, G., Boebel, O., Klatt, O., & Wisotzki, A. (2011). Warming of deep and abyssal water masses along the Greenwich meridian on decadal time scales: The Weddell gyre as a heat buffer. *Deep-Sea Research Part II Topical Studies in Oceanography*, *58*(25–26), 2509–2523. https://doi.org/10.1016/j.dsr2.2011.06.007

Fahrbach, E., & Rohardt, G. (2012). Physical oceanography and current meter data from mooring AWI207-6 [Dataset]. PANGAEA. https://doi.org/10.1594/PANGAEA.792957

Fahrbach, E., Rohardt, G., Scheele, N., Schroder, M., Strass, V., & Wisotzki, A. (1995). Formation and discharge of deep and bottom water in the northwestern Weddell Sea. *Journal of Marine Research*, *53*(4), 515–538. https://doi.org/10.1357/0022240953213089

Fogt, R. L., Bromwich, D. H., & Hines, K. M. (2011). Understanding the SAM influence on the South Pacific ENSO teleconnection. *Climate Dynamics*, *36*(7), 1555–1576. https://doi.org/10.1007/s00382-010-0905-0

Foldvik, A., Gammelsrød, T., Øterhus, S., Fahrbach, E., Rohardt, G., Schröder, M., et al. (2004). Ice shelf water overflow and bottom water formation in the southern Weddell Sea. *Journal of Geophysical Research C*, *109*(2), 1–15. https://doi.org/10.1029/2003jc002008

Foster, T. D., & Carmack, E. C. (1976). Frontal zone mixing and Antarctic Bottom Water formation in the southern Weddell Sea. *Deep Sea Research*, *23*(4), 301–317. https://doi.org/10.1016/0011-7471(76)90872-x

Fukamachi, Y., Rintoul, S. R., Church, J. A., Aoki, S., Sokolov, S., Rosenberg, M. A., & Wakatsuchi, M. (2010). Strong export of Antarctic Bottom Water east of the Kerguelen Plateau. *Nature Geoscience*, *3*(5), 327–331. https://doi.org/10.1038/ngeo842

Gordon, A. L. (1998). Western Weddell Sea thermohaline stratification. In S. Jacobs & R. Weiss (Eds.), *Ocean, ice, atmosphere: Interactions at the Antarctic continental margin*, *Antarctic research series* (Vol. 75, pp. 215–240). American Geophysical Union. https://doi.org/10.1029/ar075p0215

Gordon, A. L., Huber, B., McKee, D., & Visbeck, M. (2010). A seasonal cycle in the export of bottom water from the Weddell Sea. *Nature Geoscience*, *3*(8), 551–556. https://doi.org/10.1038/ngeo916

Gordon, A. L., Huber, B. A., & Abrahamsen, E. P. (2020). Interannual variability of the outflow of Weddell Sea bottom water. *Geophysical Research Letters*, *47*(4), 1–9. https://doi.org/10.1029/2020GL087014

Gordon, A. L., Huber, B. A., Hellmer, H. H., & Ffield, A. (1993). Deep and bottom water of the Weddell Sea's Western Rim. *Science*, *262*(5130), 95–97. https://doi.org/10.1126/science.262.5130.95

Gordon, A. L., Visbeck, M., & Huber, B. (2001). Export of Weddell Sea deep and bottom water. *Journal of Geophysical Research*, *106*(C5), 9005–9017. https://doi.org/10.1029/2000jc000281

Hattermann, T. (2018). Antarctic thermocline dynamics along a narrow shelf with easterly winds. *Journal of Physical Oceanography*, *48*(10), 2419–2443. https://doi.org/10.1175/JPO-D-18-0064.1

Hattermann, T., Nicholls, K. W., Hellmer, H. H., Davis, P. E. D., Janout, M. A., Østerhus, S., et al. (2021). Observed interannual changes beneath Filchner-Ronne Ice Shelf linked to large-scale atmospheric circulation. *Nature Communications*, *12*(1), 1–11. https://doi.org/10.1038/s41467-021-23131-x

21699291, 2023, 2, Downloaded from https://agupubs.onlinelibrary.wiley.com/doi/10.1029/2022JC019375 by Wiley, Wiley Online Library on [14/02/2023]. See the Terms and Conditions (https://onlinelibrary.wiley.com/terms-and-conditions) on Wiley Online Library for rules of use; OA articles are governed by the applicable Creative Commons License

Hellmer, H. H., Kauker, F., Timmermann, R., Determann, J., & Rae, J. (2012). Twenty-first-century warming of a large Antarctic ice-shelf cavity by a redirected coastal current. *Nature*, *485*(7397), 225–228. https://doi.org/10.1038/nature11064

Hellmer, H. H., Kauker, F., Timmermann, R., & Hattermann, T. (2017). The fate of the southern Weddell Sea continental shelf in a warming climate. *Journal of Climate*, *30*(12), 4337–4350. https://doi.org/10.1175/JCLI-D-16-0420.1

Hellmer, H. H., Schröder, M., Haas, C., Dieckmann, G. S., & Spindler, M. (2008). The ISPOL drift experiment. *Deep-Sea Research Part II Topical Studies in Oceanography*, *55*(8–9), 913–917. https://doi.org/10.1016/j.dsr2.2008.01.001

Hersbach, H., Bell, B., Berrisford, P., Hirahara, S., Horányi, A., Muñoz-Sabater, J., et al. (2020). The ERA5 global reanalysis. *Quarterly Journal of the Royal Meteorological Society*, *146*(730), 1999–2049. https://doi.org/10.1002/qj.3803

Hoppema, M. (2022). *Expedition programme PS129, Expeditionsprogramm Polarstern* (p. 55). Alfred Wegener Institute for Polar and Marine Research. Retrieved from https://epic.awi.de/id/eprint/55571/

Huang, B., Thorne, P. W., Smith, T. M., Liu, W., Lawrimore, J., Banzon, V. F., et al. (2016). Further exploring and quantifying uncertainties for extended reconstructed sea surface temperature (ERSST) version 4 (v4). *Journal of Climate*, *29*(9), 3119–3142. https://doi.org/10.1175/JCLI-D-15-0430.1

Huhn, O., Hellmer, H. H., Rhein, M., Rodehacke, C., Roether, W., Schodlok, M. P., & Schröder, M. (2008). Evidence of deep- and bottom-water formation in the western Weddell Sea. *Deep-Sea Research Part II Topical Studies in Oceanography*, *55*(8–9), 1098–1116. https://doi.org/10.1016/j.dsr2.2007.12.015

Hutchinson, K., Deshayes, J., Sallee, J. B., Dowdeswell, J. A., de Lavergne, C., Ansorge, I., et al. (2020). Water mass characteristics and distribution adjacent to Larsen C ice shelf, Antarctica. *Journal of Geophysical Research: Oceans*, *125*(4), e2019JC015855. https://doi.org/10.1029/2019JC015855

Janout, M. A., Hellmer, H. H., Hattermann, T., Huhn, O., Sültenfuss, J., Østerhus, S., et al. (2021). FRIS revisited in 2018: On the circulation and water masses at the Filchner and Ronne Ice Shelves in the southern Weddell Sea. *Journal of Geophysical Research: Oceans*, *1979*(2018), 1–19. https://doi.org/10.1029/2021jc017269

Jenkins, A. (1991). A one-dimensional model of ice shelf-ocean interaction. *Journal of Geophysical Research*, *96*(C11), 671–677. https://doi.org/10.1029/91jc01842

Johnson, G. C. (2008). Quantifying Antarctic bottom water and North Atlantic deep water volumes. *Journal of Geophysical Research*, *113*(C5), C05027. https://doi.org/10.1029/2007JC004477

Jullion, L., Jones, S. C., Naveira Garabato, A. C., & Meredith, M. P. (2010). Wind-controlled export of Antarctic bottom water from the Weddell Sea. *Geophysical Research Letters*, *37*(9), L09609. https://doi.org/10.1029/2010GL042822

Knust, R. (2017). Polar research and supply vessel POLARSTERN operated by the Alfred-Wegener-Institute. *Journal of Large-Scale Research Facilities JLSRF*, *3*, A119. https://doi.org/10.17815/jlsrf-3-163

Lefebvre, W., Goosse, H., Timmermann, R., & Fichefet, T. (2004). Influence of the southern annular mode on the sea ice—Ocean system. *Journal of Geophysical Research*, *109*(9), 1–12. https://doi.org/10.1029/2004JC002403

le Paih, N., Hattermann, T., Boebel, O., Kanzow, T., Lüpkes, C., Rohardt, G., et al. (2020). Coherent seasonal acceleration of the Weddell Sea boundary current system driven by upstream winds. *Journal of Geophysical Research: Oceans*, *125*(10), 1–20. https://doi.org/10.1029/2020JC016316

Llanillo, P. J., Kanzow, T., & Janout, M. (2023). SAM-ENSO Index (SEI) (Version 1.0) [Dataset]. Zenodo. https://doi.org/10.5281/ZENODO.7500163

Marshall, G. J. (2003). Trends in the southern annular mode from observations and reanalyzes. *Journal of Climate*, *16*(24), 4134–4143. https://doi.org/10.1175/1520-0442(2003)016<4134:TITSAM>2.0.CO;2

Marshall, J., & Speer, K. (2012). Closure of the meridional overturning circulation through Southern Ocean upwelling. *Nature Geoscience*, *5*(3), 171–180. https://doi.org/10.1038/ngeo1391

Martinson, D. G., & Iannuzzi, R. A. (2003). Spatial/temporal patterns in Weddell gyre characteristics and their relationship to global climate. *Journal of Geophysical Research*, *108*(4), 8083. https://doi.org/10.1029/2000jc000538

McDougall, T. J., & Barker, P. M. (2011). Getting started with TEOS-10 and the Gibbs seawater (GSW) oceanographic toolbox (SCOR/IAPSO WG127).

McKee, D. C., Yuan, X., Gordon, A. L., Huber, B. A., & Dong, Z. (2011). Climate impact on interannual variability of Weddell Sea bottom water. *Journal of Geophysical Research*, *116*(5), 1–17. https://doi.org/10.1029/2010JC006484

Meijers, A., Meredith, M., Abrahamsen, E., Morales Maqueda, M., Jones, D., & Naveira Garabato, A. (2016). Journal of geophysical research: Oceans wind-driven export of Weddell Sea slope water. *Journal of Geophysical Research: Oceans*, *121*(1900), 7530–7546. https://doi.org/10.1002/2016JC011757.Received

Meredith, M. P., Gordon, A. L., Naveira Garabato, A. C., Abrahamsen, E. P., Huber, B. A., Jullion, L., & Venables, H. J. (2011). Synchronous intensification and warming of Antarctic Bottom Water outflow from the Weddell Gyre. *Geophysical Research Letters*, *38*(3), 2–5. https://doi.org/10.1029/2010GL046265

Meredith, M. P., Renfrew, I. A., Clarke, A., King, J. C., & Brandon, M. A. (2004). Impact of the 1997/98 ENSO on upper ocean characteristics in Marguerite Bay, western Antarctic Peninsula. *Journal of Geophysical Research*, *109*(C9), 1–19. https://doi.org/10.1029/2003JC001784

Muench, R., & Hellmer, H. (2002). The international DOVETAIL program. *Deep Sea Research II*, *49*(21), 4711–4714. https://doi.org/10.1016/s0967-0645(02)00155-8

Muench, R. D., & Gordon, A. L. (1995). Circulation and transport of water along the western Weddell Sea margin. *Journal of Geophysical Research*, *100*(C9), 18503. https://doi.org/10.1029/95jc00965

Naveira Garabato, A. C., McDonagh, E. L., Stevens, D. P., Heywood, K. J., & Sanders, R. J. (2002). On the export of Antarctic Bottom Water from the Weddell Sea. *Deep-Sea Research Part II Topical Studies in Oceanography*, *49*(21), 4715–4742. https://doi.org/10.1016/S0967-0645(02)00156-X

Nicholls, K. W., Makinson, K., & Robinson, A. V. (1991). Ocean circulation beneath the Ronne Ice Shelf. *Nature*, *354*(6350), 221–223. https://doi.org/10.1038/354221a0

Nicholls, K. W., & Østerhus, S. (2004). Interannual variability and ventilation timescales in the ocean cavity beneath Filchner-Ronne Ice Shelf, Antarctica. *Journal of Geophysical Research C*, *109*(4), 1–9. https://doi.org/10.1029/2003JC002149

Nicholls, K. W., Østerhus, S., Makinson, K., Gammelsrød, T., & Fahrbach, E. (2009). Ice-ocean processes over the continental shelf of the southern Weddell Sea, Antarctica: A review. *Reviews of Geophysics*, *47*(3), 1–23. https://doi.org/10.1029/2007RG000250

Orsi, A. H. (2010). Oceanography: Recycling bottom waters. *Nature Geoscience*, *3*(5), 307–309. https://doi.org/10.1038/ngeo854

Orsi, A. H., Jacobs, S. S., Gordon, A. L., & Visbeck, M. (2001). Cooling and ventilating the abyssal ocean. *Geophysical Research Letters*, *28*(15), 2923–2926. https://doi.org/10.1029/2001GL012830

Orsi, A. H., Johnson, G. C., & Bullister, J. L. (1999). Circulation, mixing, and production of Antarctic Bottom Water. *Progress in Oceanography*, *43*(1), 55–109. https://doi.org/10.1016/S0079-6611(99)00004-X

21699291, 2023, 2, Downloaded from https://agupubs.onlinelibrary.wiley.com/doi/10.1029/2022JC019375 by Wiley, Wiley Online Library on [14/02/2023]. See the Terms and Conditions (https://onlinelibrary.wiley.com/terms-and-conditions) on Wiley Online Library for rules of use; OA articles are governed by the applicable Creative Commons License

Purich, A., & England, M. H. (2021). Historical and future projected warming of Antarctic shelf bottom water in CMIP6 models. *Geophysical Research Letters*, *48*(10), e2021GL092752. https://doi.org/10.1029/2021GL092752

Reid, J. L., & Lynn, R. J. (1971). On the influence of the Norwegian-Greenland and Weddell seas upon the bottom waters of the Indian and Pacific oceans. *Deep-Sea Research and Oceanographic Abstracts*, *18*(11), 1063–1088. https://doi.org/10.1016/0011-7471(71)90094-5

Rohardt, G., & Boebel, O. (2017). Physical oceanography and current meter data from mooring AWI207-8 [Dataset]. PANGAEA. https://doi.org/10.1594/PANGAEA.875124

Rohardt, G., & Boebel, O. (2019a). Physical oceanography and current meter data from mooring AWI257-1 [Dataset]. PANGAEA. https://doi.org/10.1594/PANGAEA.898718

Rohardt, G., & Boebel, O. (2019b). Physical oceanography and current meter data from mooring AWI258-1 [Dataset]. PANGAEA. https://doi.org/10.1594/PANGAEA.898762

Rohardt, G., & Boebel, O. (2019c). Physical oceanography and current meter data from mooring AWI259-1 [Dataset]. PANGAEA. https://doi.org/10.1594/PANGAEA.898791

Rohardt, G., & Boebel, O. (2019d). Physical oceanography and current meter data from mooring AWI260-1 [Dataset]. PANGAEA. https://doi.org/10.1594/PANGAEA.898792

Rohardt, G., & Boebel, O. (2019e). Physical oceanography and current meter data from mooring AWI207-10 [Dataset]. PANGAEA. https://doi.org/10.1594/PANGAEA.898777

Rohardt, G., & Boebel, O. (2019f). Physical oceanography and current meter data from mooring AWI261-1 [Dataset]. PANGAEA. https://doi.org/10.1594/PANGAEA.898793

Rohardt, G., & Boebel, O. (2019g). Physical oceanography and current meter data from mooring AWI262-1 [Dataset]. PANGAEA. https://doi.org/10.1594/PANGAEA.898794

Ryan, S., Hattermann, T., Darelius, E., & Schröder, M. (2017). Seasonal cycle of hydrography on the eastern shelf of the Filchner Trough, Weddell Sea, Antarctica. *Journal of Geophysical Research: Oceans*, *122*(8), 6437–6453. https://doi.org/10.1002/2017JC012916

Ryan, S., Hellmer, H. H., Janout, M., Darelius, E., Vignes, L., & Schröder, M. (2020). Exceptionally warm and prolonged flow of warm deep water toward the Filchner-Ronne Ice Shelf in 2017. *Geophysical Research Letters*, *47*(13), e2020GL088119. https://doi.org/10.1029/2020GL088119

Schröder, M., Hellmer, H., & Absy, J. (2002). On the near-bottom variability in the northwestern Weddell Sea. In *Deep-sea research II* (Vol. 49).

Spence, P., Griffies, S. M., England, M. H., Hogg, A. M., Saenko, O. A., & Jourdain, N. C. (2014). Rapid subsurface warming and circulation changes of Antarctic coastal waters by poleward shifting winds. *Geophysical Research Letters*, *41*(13), 4601–4610. https://doi.org/10.1002/2014GL060613

Stammerjohn, S. E., Martinson, D. G., Smith, R. C., Yuan, X., & Rind, D. (2008). Trends in Antarctic annual sea ice retreat and advance and their relation to El Niño–Southern Oscillation and Southern Annular Mode variability. *Journal of Geophysical Research*, *113*(C3), C03S90. https://doi.org/10.1029/2007JC004269

Stommel, H. (1958). The abyssal circulation. *Deep Sea Research (1953)*, 5(1), 80–82. https://doi.org/10.1016/S0146-6291(58)80014-4

Stommel, H., & Arons, A. B. (1959). On the abyssal circulation of the world ocean--I. Stationary planetary flow patterns on a sphere. 140–154.

Thompson, A. F., & Heywood, K. J. (2008). Frontal structure and transport in the northwestern Weddell Sea. *Deep-Sea Research Part I Oceanographic Research Papers*, *55*(10), 1229–1251. https://doi.org/10.1016/j.dsr.2008.06.001

Thompson, D. W. J., & Solomon, S. (2003). Interpretation of recent southern Hemisphere climate change. *Scienc*e, *302*(5643), 273–275. https://doi.org/10.1126/science.1087440

van Caspel, M., Schröder, M., Huhn, O., & Hellmer, H. H. (2015). Precursors of Antarctic bottom water formed on the continental shelf off Larsen Ice Shelf. *Deep-Sea Research Part I Oceanographic Research Papers*, *99*, 1–9. https://doi.org/10.1016/j.dsr.2015.01.004

van Heuven, S., Hoppema, M., Jones, E., & de Baar, H. (2014). Rapid invasion of anthropogenic CO_2 into the deep circulation of the Weddell Gyre. *Philosophical Transactions of the Royal Society A: Mathematical, Physical & Engineering Sciences*, *372*(2019), 20130056. https://doi.org/10.1098/rsta.2013.0056

Warren, B. (1981). Deep circulation of the world ocean. In B. A. Warren & C. Wunsch (Eds.), *Evolution of physical oceanography* (pp. 6–41). MIT Press.

Yuan, X. (2004). ENSO-related impacts on Antarctic sea ice: A synthesis of phenomenon and mechanisms. *Antarctic Science*, *16*(4), 415–425. https://doi.org/10.1017/S0954102004002238

Erratum

In the originally published version of this article, in the fourth paragraph of section 5.4, the text reads: "In the case of the northwestern Weddell Sea, the weakening of the northerlies in the eastern side of the Antarctic Peninsula . . . . In this regard, the observation-based SAM Index (Marshall, 2003) was markedly negative . . . . This is reflected in ERA5 wind reanalysis data (Hersbach et al., 2020) by weaker easterlies in the southern Weddell Sea and weaker northerlies in the western Weddell Sea . . . ." The two instances of "northerlies" should be "southerlies." These errors have been corrected, and this may be considered the authoritative version of record.

21699291, 2023, 2, Downloaded from https://agupubs.onlinelibrary.wiley.com/doi/10.1029/2022JC019375 by Wiley, Wiley Online Library on [14/02/2023]. See the Terms and Conditions (https://onlinelibrary.wiley.com/terms-and-conditions) on Wiley Online Library for rules of use; OA articles are governed by the applicable Creative Commons License